Chem Soc Rev

REVIEW ARTICLE

View Article Online
View Journal | View Issue

Cite this: *Chem. Soc. Rev.*, 2021, **50**, 7108

Rapid hybrid perovskite film crystallization from solution

Sandy Sánchez, *[ab] Lukas Pfeifer, [b] Nikolaos Vlachopoulos [a] and Anders Hagfeldt *[a]

The use of a solution process to grow perovskite thin films allows to extend the material processability. It is known that the physicochemical properties of the perovskite material can be tuned by altering the solution precursors as well as by controlling the crystal growth of the film. This advancement necessarily implies the need for an understanding of the kinetic phenomena for the thin-film formation. Therefore, in this work we review the state of the art of perovskite hybrid crystal growth, starting from a comprehensive theoretical description towards broad experimental investigations. One part of the study focuses on rapid thermal annealing as a tool to control nucleation and crystal growth. We deduce that controlling crystal growth with high-precision photonic sintering simplifies the experimental framework required to understand perovskite crystallization. These types of synthesis methods open a new empirical parameter space. All this knowledge serves to improve the perovskite synthesis and the thin films' quality, which will result in higher device performances.

Received 4th November 2020

DOI: 10.1039/d0cs01272f

rsc.li/chem-soc-rev

1. Introduction

Hybrid perovskite semiconductor materials have become of great interest in materials science, with an enormous potential to revolutionize the entire field and with promising applications such as thin film solar cells.[1–3] However, scaling up perovskite solar cells (PSCs) for industrial production is a complex task for this young technology, mainly due to the poor stability of the material.[4–8] All the perovskite chemical compositions are water soluble, which means that in normal environmental conditions (more than 25% of relative humidity), these lead-halide perovskites tend to degrade.[9] Numerous approaches have been proposed to overcome this problem, and the different strategies can be divided into essentially three categories: 1 – chemical passivation; 2 – compositional engineering; and 3 – new synthesis methods.[10–12]

[a] *Laboratory of Photomolecular Sciences, Institute of Chemistry and Chemical Engineering, École Polytechnique Fédérale de Lausanne, 1015 Lausanne, Switzerland. E-mail: sandy.sanchezalonso@epfl.ch, anders.hagfeldt@epfl.ch*
[b] *Laboratory of Photonics and Interfaces, Institute of Chemistry and Chemical Engineering, École Polytechnique Fédérale de Lausanne, 1015 Lausanne, Switzerland*

Sandy Sánchez

Sandy Sanchez received his PhD degree in Physics in 2019 from the University of Fribourg, Switzerland, under the guidance of Prof. Ullrich Steiner. He then joined the group of Prof. Anders Hagfeldt at EPFL, Switzerland. His research interests concern semiconductor physics, solar cells and solidification process. Specifically, he has worked in hybrid perovskite materials for thin-film crystallization with photonic sintering.

Lukas Pfeifer

Lukas Pfeifer obtained his PhD from the University of Oxford in 2017 for his work on novel reagents and methods for C–F bond formation carried out under the guidance of Prof. V. Gouverneur. He then joined the Feringa group at the University of Groningen as a postdoctoral researcher focussing on the development of near-infrared light-driven rotary molecular motors. In 2020, he joined the Laboratory of Photonics and Interfaces of Prof. Michael Grätzel at EPFL where he is working on the stability and performance of dye-sensitized and perovskite solar cells.

The three mentioned strategies focus on removing crystal defects, either from the bulk or from the surface. The selecting layers and the final chosen architecture are as well part of the problem to be solved, however the perovskite itself not only attracts the most attention, it is also the fundamental component in the cell. This is the major reason why this review focuses on perovskite crystallization, in order to give a comprehensive overview of what has been accomplished that can provide paths to overcome the stability issues in PSCs. A defect-tolerant perovskite film has less chance to be degraded, since interstitial defects and deeps traps, among others, as non-radiative centres have a major cause in the crystallization mechanism.[13,14] The change of microstrain in the perovskite lattice can be first determined by defects during crystal nucleation and growth, which can be further detrimental by external stress factors like humidity, photodegradation, and temperature.[15,16] These defects will have direct consequences in ion migration, non-radiative recombination, and organic decomposition, being examples of mechanisms triggering irreversible degradation pathways.[17–20]

We believe that a new theoretical framework is needed to understand a complex phenomena of perovskite crystallization, which occurs far from thermodynamic equilibrium.[21] Therefore, this review relates the perovskite kinetic phenomena with new fabrication procedures and different theoretical approaches as for example the dendrite growth, very known in the polymers field.[22,23] Thus this review is compiled in three parts, the state of the art of perovskite nucleation and crystal growth, from a more theoretical approach, passing through rapid or controlled growth to phase evolution during crystal growth. The two last sections rely in a more experimental style, to review the structural evolution, the final crystal shape and its relationship with crystallization method, the latter more detailed in section two.

Looking for alternatives to deposit a defect-tolerant perovskite film, this review discusses in-depth a synthesis method called flash infrared annealing (FIRA).[24–28] This method is based on thermal rapid processing, which has been widely employed to synthesize thin films for semiconductor applications.[29–32] For deeply exploiting FIRA, an understanding of the thin-film crystallization phenomenon is needed. From FIRA optimization parameters to experimental approaches, this review addresses how to rapidly produce defect-tolerant perovskite thin films that enables the manufacturing of highly efficient solar cells. The kinetics of the nucleation and crystal growth process is also addressed, based on several fundamental studies of particular FIRA cases, disclosing the mechanism involved in driving film crystallization. These fundamental studies have the aim to use FIRA for manufacturing stable PSCs, increasing their power conversion efficiency (PCE), and enabling the scale-up to the industry of this technology.

2. Crystal nucleation and growth from solution

2.1. Thermodynamic of nucleation and crystal growth

A nucleus can be defined as the minimum amount of a new phase, which can be a cluster of few atoms or molecules. A first-order phase transition mechanism is the formation of incipient crystallization nuclei in an initial metastable phase. The diffusion of particles rules the crystal growth step, which directly follows the nucleation. While, as growing clusters on the nuclei's surface follow later integration in the crystal lattice structure.[33,34] In perovskite solutions, as the solvent evaporates, the precursor changes the chemical potential, eventually reaching supersaturation to allow a new phase through crystal growth. Nucleation is promoted by the supersaturation state, with the formation of nuclei-clusters that favored crystal growth. Nucleation processes have Gibbs energetic barriers that need to be surpassed. These barriers are a function of the critical nucleus size.[35]

The relationship between supersaturation and the critical nucleus size inducing crystal growth can be described in terms of the Gibbs free energy of the system. Assume that a spherical nucleus cluster is formed on a substrate surface, with r as the nuclei radius, θ the contact angle which the nucleus forms with the substrate, ΔG_v the Gibbs free energy per unit volume, γ_0 the nucleus surface tension, γ_1 the nucleus–substrate interfacial tension, and γ_2 the substrate surface tension. In equilibrium, Young's equation is given by:

$$\gamma_0 \cos\theta = \gamma_2 - \gamma_1. \tag{2.1}$$

The change in surface and interfacial Gibbs free energy can be expressed as[33]

$$G_s 2\pi r^2(1 - \cos\theta)\pi(r\sin\theta)^2(\gamma_1 - \gamma_2) = \pi r^2\gamma_0(2 - 3\cos\theta + \cos^3\theta). \tag{2.2}$$

For the spherical cap nucleus, its volume V is

$$V = \frac{\pi r^3(2 - 3\cos\theta + \cos^3\theta)}{3}. \tag{2.3}$$

Therefore, the change of the volume free energy is

$$\Delta G_V = V \cdot \Delta G_V = \frac{\pi r^3(2 - 3\cos\theta + \cos^3\theta)}{3}\Delta G_V, \tag{2.4}$$

and the change of total free energy is

$$\Delta G = \Delta G_s + \Delta G_V = \pi\left(\frac{r^3}{3}\Delta G_V + r^2\gamma_0\right)(2 - 3\cos\theta + \cos^3\theta). \tag{2.5}$$

Setting:

$$\frac{\partial(\Delta G)}{\partial r} = 0, \tag{2.6}$$

the critical nucleus radius is given by:

$$r_0 = \frac{-2\gamma_0}{\Delta G_V}(\Delta G_V < 0). \tag{2.7}$$

Since ΔG_v is the energy needed from equilibrium state to supersaturation, it can be expressed as:

$$\Delta G_V = -Z(T)\cdot\ln\left(\frac{\rho_s}{\rho_e}\right), \tag{2.8}$$

where $Z(T)$ is a temperature and growth-type dependent coefficient (shape of the stable clusters), ρ_s is the concentration

corresponding to supersaturation and ρ_e is the equilibrium concentration.[33] For stable nuclei formations, an increase of the interfacial energy is needed due to the solid–liquid interface balance, where an energy decrease is rendered by the formation of a thermodynamically stable new solid phase. However, a shallow nucleation rate can result from low supersaturations, and therefore the formation of an unstable cluster, whereby the energy released is less than that required for the formation of a liquid–solid interface.[36]

A significant empirical contribution was given by von Weimarn,[37] where the size of the precipitated particle is inversely proportional to the relative supersaturation state. The von Weirmarn rules for solutions imply how the precursors can react with different solvents to decrease/increase the solubility and emphasizes the average crystal size dependence on the supersaturation state. However, for precursor solutions other phenomena influencing the solubility are present and can be described by theories such as that of Lewis acidity-base behavior, as we will discuss herein.[38] Supersaturation can be defined by the relation of solution concentration with respect to the equilibrium concentration at the same temperature:

$$\xi = \frac{\rho_s}{\rho_e} - 1 \tag{2.9}$$

with the free energy needed for the equilibrium state ΔG_v given by

$$\Delta G_V = Z(T)\ln(\xi + 1). \tag{2.10}$$

Based on the above relation, the critical nucleus radius can be expressed as

$$r_0 = \frac{2\gamma_0}{Z(T)\ln(\xi + 1)}. \tag{2.11}$$

As supersaturation is reached, the balance of chemical potentials can result in the surpassing of the nucleation barrier for certain nuclei sizes. The free energy changes are associated with the formation of the nuclei and are a consequence of the formation of the new phase.[39] On the surface, the interaction of molecules in solution with their neighbors differs from those in mass. Meanwhile, its contribution to the new stage's free energy varies and is usually more prominent in this manner. Therefore, the interfacial energy is given by the difference between the free energy per molecule in bulk and in the surface.[40,41]

A critical nucleus size is required for a nucleus to form from a supersaturated solution, which has a number of implications, as previously discussed. The critical size of the new phase is reached due to variations that add sufficient amounts of molecules. Therefore, the value of the critical size influences the nucleation probability.[42] In parallel, nucleation is a function of interfacial energy, which has a direct relationship. Consequently, the interfacial energy or the probability of nucleation can be manipulated by modulating the nucleus's critical size.[33]

2.2. Crystal nucleation and growth

2.2.1. Homogeneous and heterogeneous nucleation. Departing from a uniform solution in an initial state, the transformation rate depends on the atomic or molecular composition, the reaction kinetic and the heat flow at the interface. A first-order phase-transition mechanism governs an initial metastable nuclei phase.[41] In nature, almost all the nucleation processes are heterogeneous and may depend on the nucleating agent involved.[43] For instance, in perovskite solar cells Dongqin Bi *et al.*[44] have reported a polymer-templated (adding PMMA in the antisolvent solution) to allow a heterogeneous nucleation and crystal perovskite growth that enhances the PCE of the cell. In homogeneous nucleation, solely the material that crystallizes is involved, being an intrinsic material's process. Although the conditions to initiate nucleation are the limits of the amorphous phase stability, resulting in much further difficulty in the interior of a uniform substance. Homogeneous nucleation can be analyzed more readily than heterogeneous nucleation that involves a foreign, often unknown, material. Heterogeneous nucleation forms at preferential sites such as phase boundaries, surfaces, or impurities like dust.[45,46] The free energy barrier can be reduced by lowering the effective surface energy at the preferential sites, promoting nucleation. The wetting facilitates nucleation at the surface for contact angles higher than zero. Therefore, the product of homogeneous nucleation and a function of the contact angle is equal to Gibbs free energy necessary for heterogeneous nucleation Θ:

$$\Delta G^*_{\text{heterogeneous}} = \Delta G^*_{\text{heterogeneous}} \cdot f(\Theta) \tag{2.12}$$

where:

$$f(\Theta) = \frac{2 - 3\cos\theta + \cos^3\theta}{4} \tag{2.13}$$

Fig. 1a shows the contribution of the interfacial energy and the volume for the total free energy needed to form a stable nucleus, as stated in eqn (2.5). Then, in Fig. 1b the two energy barriers related to the formation of a nucleus for homogeneous and heterogeneous nucleation can be seen as a function of the critical radius. The wetting effect determines the nucleation's feasibility by lowering the energy barrier.

2.2.2. Kinetics of the reaction. For solution processes, the nature of the reactants, such as the acid–base reactions, can determine the transformation into product as well as the strength of the bonds of the chemical species involved.[47] In addition, specific experiences for perovskite halide will be addressed in the next section. In a chemical reaction the pathway of the transformation of the species involved toward the product can be kinetically described by means of a reaction rate.[48,49] In the steady state condition, the rate of reaction will depend on a specific area and the frequency of collisions between molecules or ions. In order for the kinetic rate expression to correspond to the stoichiometry, it has to be elementary at the molecular level, mostly monomolecular or bimolecular. For the overall (multistep) reaction involving the formation and breakdown of molecular complexes, corresponding to a series

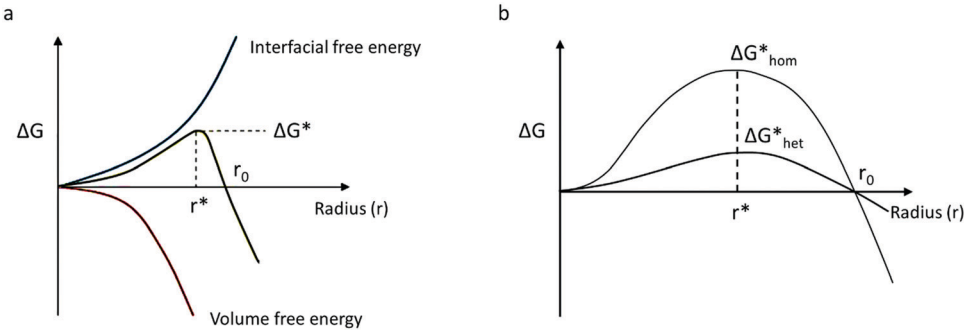

Fig. 1 (a) Relationship between volumetric and interfacial energy for the energy barrier to form a nucleus. (b) Energetic barriers for homogeneous and heterogeneous nucleation.

of many elementary reactions, intermediate species play a key role as reactants.[41] The intermediate reactants are fundamental for the kinetic study of complex reactions, since the product of the reaction cannot be predicted just from the stoichiometry of the reactants.

For reaction rates treatment, the temperature is one of the most important variables due to its exponential dependence, as expressed in the Arrhenius equation proposed in 1889:[50]

$$K = A\exp\left(-\frac{E_a}{RT}\right) \tag{2.14}$$

where E_a is the activation energy of the reaction, A pre-exponential factor and R the gas constant. Therefore, activation energies of the overall reaction can easily be fitted by the plot of $\ln K$ *versus* $1/T$. The empirical nature of the Arrhenius equation does not consider any mechanistic description of the intermediates species involved and only involves the macroscopic constant rate for a given reaction.[51] The energy activation of an overall reaction is the composite of many activation energies from elementary reactions. Thus, the transition state theory based on statistical mechanics portrays a multidimensional potential surface related to the energy variation as a function of the atom positions for a given reaction.[41] The size of the activation energy is a fundamental variable for controlling the rates in processes, and it can be derived from the maximum of the potential surface of the reaction corresponding to the variation of the Gibbs free energy *vs.* the generalized position coordinate of the reacting species. Therefore, the potential energy surface topology is an accurate description of the activated complex related to such intermediate reactive species.[52]

2.2.3. Nucleation rate. The equilibrium number of critical size nuclei and the atoms' frequency that favorably transfers into the nucleus phase gives the nucleation rate.[53] The nucleation rate, J, is then the product of a thermodynamic barrier described by ΔG^* and a kinetic barrier k_BT, given by the rate of atomic attachment. The Volmer–Weber (1925) model,[54,55] assumes that clusters are isolated spheres, but is also applicable for the critical size of whatever shape. Accordingly, following the Arrhenius approach, the rate law J is given by:[54,55]

$$J \propto A\exp\left(\frac{\Delta G^*}{k_BT}\right) \tag{2.15}$$

This means that the formation of a new phase contradicts the cluster separation assumption, which makes it impossible to analytically obtain the cluster distribution. The kinetic factor depends on the molecular mobility, being related to the attachment's rate of molecules to the nucleus. While the pre-exponential factor A is a remarkable assumption because of its dependence on temperature and its relationship to rapid molecular mobility changes.[56]

In a phase transformation process the energy of the atoms can follow the Maxwell–Boltzmann distribution. If n_0 is the density of atoms in a liquid and n_R is the density of cluster in equilibrium with the liquid, then:

$$\frac{n_r}{n_0} = \exp\left(-\frac{\Delta G^*}{k_BT}\right) \tag{2.16}$$

A cluster with a critical radius size r_0 will grow when more atoms can be added and the rate of growing will be proportional to the atomic vibration frequency ν_0 and the probability of adding another atom to the surface σ. Then the homogeneous nucleation rate is given by:

$$J^{homo} = \nu_0\sigma n_r = \nu_0\sigma n_0\exp\left(-\frac{\Delta G^*}{k_BT}\right) \tag{2.17}$$

and for heterogeneous nucleation rate the factor $f(\theta)$ can be added, according to eqn (2.13):

$$J^{hetero} = \nu_0\sigma n_r = \nu_0\sigma n_0\exp\left(-\frac{\Delta G^*}{k_BT}f(\theta)\right) \tag{2.18}$$

The nucleation rate for homogeneous nucleation strongly depends on temperature, but in the case of heterogeneous nucleation the factor $f(\theta)$ is also determining, which relates the contact angle and the radius of a spherical cluster. Therefore, the nucleation rate for heterogeneous nucleation also depends on the type of a foreign substrate.[56]

2.2.4. Nucleation and growth. The whole heterogeneous nucleation phenomena can be analysed by a combination of primary and secondary nucleation processes. Secondary nucleation occurs because of the presence of seed-crystals of the material being crystallized, where nuclei are formed at the surface of bigger clusters.[57,58] Maggioni *et al.*[59] presented a new model, which describes unseeded nucleation and crystallization of a species exhibiting an arbitrary number of polymorphs, as represented in Fig. 2. The model considers each new primary as

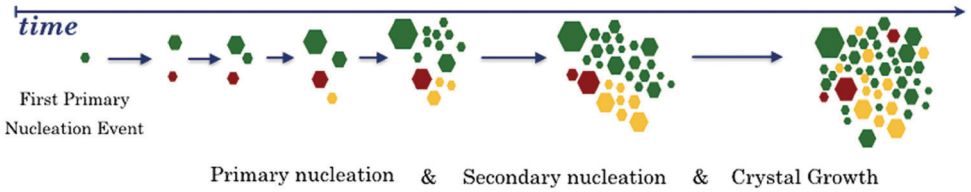

Fig. 2 Schematic representation of the crystallization of a system with three different polymorphs (reproduced with permission from ref. 58. ©2019 American Chemical Society).

a nucleus's stochastic formation and, adopting the population balance equations framework, further describes crystal growth and secondary nucleation deterministically.[59]

The growth stage, which follows nucleation, is produced by the diffusion of the particles to the surface of the existing nucleus and their integration into the crystal lattice structure. The initial stages of solution crystallization determine the crystal's properties, mainly the size distribution and the crystal structure.[21] For crystal growth, the main assumption is that stable nuclei exist prior to growth, adding molecules to a stable cluster driven by the decrease of the Gibbs free energy of the phase, with the change kinetically limited. The crystal shape can be analyzed by the Johnson–Mehl–Avrami equation,[34,60] where the volume transformation x as a function of time of a new β-phase is given by:

$$x(t) = 1 - \exp[-(\beta)^N] \tag{2.19}$$

The parameter N depends on the shape of β-phase particles. For example, as regards different dimensions it is $N = 3$, $N = 2$, and $N = 1$ for sphere-, disk-, and rod-shaped particles, respectively.

At the beginning and the end of the process, the transformation rates are low but fast in-between. The time required for a sufficient nuclei formation for the new phase is due to the early slow rate. The transformation accelerates in the intermediate stage when the nuclei begin to grow into new particles. The new nuclei continue to form in an initial phase while the rest are incorporated into the growth phase.[34,35] When the transformation is almost complete, there is still an untransformed nuclei material that slows down new particles' production. Then the grown particles begin to form boundaries between them (where the particle ends its growth).

The Johnson–Mehl–Avrami equation can be applied to the crystallization process in a variety of amorphous solids under isothermal conditions. Thus, to support interpretations of physicochemical mechanisms derived from the obtained kinetic parameters.[61] During continuous heating, an isothermal process cannot be efficiently separated from the grain growth and crystallization process because it results in nanometers grain size. Consequently, the kinetic parameters obtained from an isothermal process apply more to a crystallization process.

A population balance equation is commonly used to obtain the population density n for any given value of crystal size, r. Randolph and Larson,[62] has defined n as:

$$n = \frac{\mathrm{d}N}{\mathrm{d}L} \tag{2.20}$$

where N is the number of crystals with size L. The crystal size depends on the linear growth v_c of crystal in the medium, meaning the change of n with L, and the population balance can be written as:

$$\frac{\partial n}{\partial t} = v_c \frac{\partial n}{\partial L} \tag{2.21}$$

The population balance in a form of the continuity equation gives the time evolution of the crystal size distribution for a closed system.[63,64] Constant rates of crystal nucleation and growth can be derived for reactions of chemical species involved.

2.3. Surface and crystallization

The driving force for the crystallization process depends on supersaturation, which is fundamental to the crystal growth rate.[17,22,28] Crystal growth kinetics is a complex phenomenon, which usually takes place through an intermediate phase. Overall, fast nucleation can improve the extent of coverage of films, and the control of the crystal growth can contribute to form a highly crystalline material.[29–32] To grow a crystal, a cluster has to be transported to the crystal surface and may have to rearrange to fit the lattice structure. The critical cluster is the equivalent of an activated complex in transition state theory. It can result in successive transport through solution and surface reaction processes. Both of these processes can be growth rate-controlling. The cluster transport can be controlled by diffusion, which is mass transport as a consequence of the thermal motion of the molecules, and by convection, which is mass movement due to an energy gradient in the system. Surface-controlled growth can be determined by nucleation and dislocation growth.[25,33,34]

2.3.1. Surface crystallization. For surface crystallization, the Kossel–Stranski model stipulates that growth clusters surrounding a crystal surface do not directly join the lattice but are adsorbed and diffuse over the surface.[65] The rate of the molecules reaching the surface from the bulk will differ from the rate of the molecules diffusing into the lattice, which depends on the number of adjacent crystal sites. The possible lattice sites for the attachment of adsorbed atoms on the crystal surface are terrace, ledge and kink site.[66] The binding energy between an adatom and an existing lattice increases from terrace to ledge to kink site.

A major drawback of the Kossel–Stranski theory is that the accumulation of atoms in the kinked ledge to diffuse to the edge of the crystal would not correspond to a low energy nucleation site. Nevertheless, a continuous source of steps that can increase over to the crystal's surface can be provided by screw dislocations.[67,68] The mechanism for step generation and

transport was elucidated by Burton, Cabrera and Frank, in a crystal growth theory.[69] An step on the crystal surface can be promoted by a screw dislocation with a size related to the lattice distortion vector's projection (Burgers vector) resulting from a dislocation.[70,71] In this theory, additional growth can occur when there is a rotation of the step throughout the dislocation point.

2.3.2. Ostwald ripening. Ostwald ripening occurs when a small particle is dissolved or coalesced into bigger particles. In simple systems, the surface energy density can be assumed independent of the shape, thus surface energy is directly proportional to surface tension.[72] The interfacial curvature effect on particle size (through energy changes) modify the solubility of the largest growth particles, being dissolved by the smaller particles; these denucleated particles will contribute to the growth and coarsening of larger particles.

Carl Steefel and Van Cappellen,[73] have developed a new kinetic approach unveiling the role of nucleation, precursors and Oswalt ripening by using the balance population equation to calculate crystal size distribution. Assuming the conservation of mass and volume, they decouple the changes in population density due to the ripening of growth and dissolution, then the continuity equation is given by:

$$\frac{\partial n}{\partial t} = v_c \frac{\partial}{\partial L}[v_{ost}(r)V] \quad (2.22)$$

where V is the volume density of the crystals and v_{ost} is the Ostwald ripening rate as a function of the grain size L. The ripening rate v_{ost} is applied to crystal distribution and represents a rate at which smaller particles combine to form crystals of larger size.

It has been reported that the Oswalt ripening effect can be used as a tool to suppress defects at the grain boundary during perovskite crystal growth,[74,75] where the aging effect tends to remove defects in perovskite films. However, due to the complexity of the ripening ratio and coarsening, the above model has to be complemented with a better experimental framework description.

2.4. Dendrite growth

In general, short time annealing at high temperature can result in an energy process equivalent to the longer annealing at a lower temperature. However, different activation energies or driving forces are necessary to reach the supersaturated state in both cases; therefore, they depend differently on the temperature.[22] For rapid thermal annealing at high temperatures, the controlled growth rate depends mainly on the thermal convection. The final crystalline morphology can be molded by the temperature gradient of the thermal process. The crystalline microarrangement will depend on the interfacial energy and the different chemical potential in the molecules (*i.e.*, crystal growth from solution), where instabilities can provide a different directional growth, led by their anisotropy. This is the case of dendritic growth, where a metastable phase can grow in an energetically favorable direction, different from the final phase.[61]

Therefore, it is of our interest to briefly introduce dendrite growth, which is the main morphological feature of the hybrid perovskites processed with the FIRA method.[24] Rapid kinetic processes can result in dendrite growth, where diffusion processes can govern the phase transformation rate. Dendrites typically grow along energetically favorable crystallography directions. Dendrites require some anisotropy, usually of the interfacial energy between crystal and solution, but this could also be anisotropy of the attachment kinetics for non-metallic systems.[76] Due to this anisotropy, dendrites can grow with different velocity, which causes the formation of stem and tips. This growth velocity mainly depends on the different diffusional processes converging, where thermal diffusivities involve faster growths.

2.4.1. Surface energy anisotropy. The equilibrium condition for liquid and solid particle of mean curvature ε can be solved for the case of isotropic interfacial energy *via* the Gibbs–Thomson equation, as written in the form:[61]

$$T_f^R = T_f^\infty - 2\Gamma_{sl}\varepsilon \quad (2.23)$$

where T_f^R is the melting point of a curved solid, which is lower than T_f^∞, the temperature of the planar solid, and Γ_{sl} is the Gibbs–Thomson coefficient.

Surface energy and atomic attachment kinetics can determine the extent to which the system is far from equilibrium with respect to the isotropic interfacial energy the conditions for equilibrium at the liquid/solid interface. Isotropicity in the systems means that the molar free Gibbs energy is constant everywhere; the crystal, therefore, is spherical. Following this, the equilibrium at the interface can be determined by the interfacial energy as a measure of the degree of anisotropy, which becomes a function of the surface normal η.[77]

The surface energy can be expressed in the form of:

$$\gamma_{sl} = \gamma_{sl}^0[1 + \varepsilon_\eta \cos(\eta\Theta)] \quad (2.24)$$

where Θ is the angle between the local surface normal vector and a chosen reference direction in the crystal and ε_η represent the strength of the anisotropy. The surface stiffness can be determined from precursor reactions, giving the equilibrium shape of the crystal, also known as Wulff construction.[78,79] There are some angles for which the surface stiffness can be negative, representing thermodynamically forbidden directions for crystal growth and thereby defining the anisotropy of the crystal. The surface energy and its anisotropy play a significant role in dendritic growth, leading to the microstructural arrangements of the crystal shape in equilibrium.[61]

Three dimensional Wulff constructions can be extrapolated in polar coordinates, as can be seen in Fig. 3a for different crystal shapes.[80] The Wulff construction can determine the surface energy as a function of the growth orientation. Experimentally, surface energies are indirectly determined from surface tension measurements, which are made in the liquid phase and then extrapolated to zero temperature without relation to any particular orientation. However, computed methods can be used to simulate the growth and shape of the materials as a dimension of anisotropy, such as phase-field models.[81–83] For instance, Y. Lu *et al.*,[84] have simulated three-dimensional free dendritic growth of a pure material in the presence of fluid flow, as can be seen in Fig. 3b. In this study, the dendrite tip growth without domain

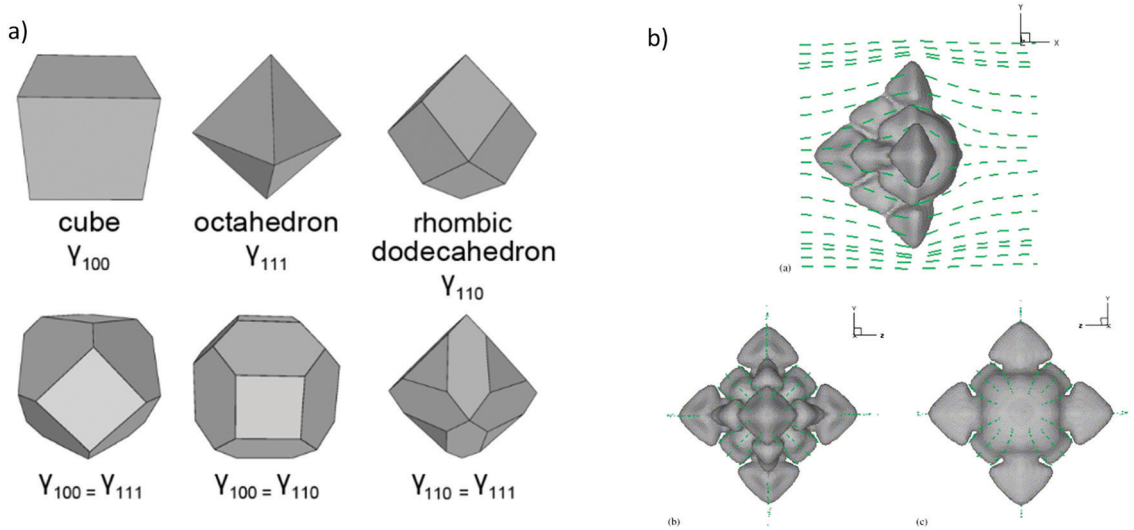

Fig. 3 (a) Common Wulff constructions for materials with full cubic symmetry (reproduced with permission from ref. 79, Creative Commons License). (b) Computed dendrite morphology with directions heat flow, (a), (b) and (c) different views of the 3D construction (reproduced with permission from ref. 83, ©2005 Published by Elsevier B.V.).

boundary interfering on thermal and velocity boundary layers can reach a steady state. Hence, tips growing in different directions to the streamflow cannot reach a steady-state regime, allowing more realistic scenarios, where the parabolic dendrite tip radius can be insufficient as we will discuss in the next subsection.

This topic can be summarized by following the "rules of thumb" for crystal growth. Firstly, the maximum surface energy is relevant to the case when the crystal seeks to minimize its total surface energy, which can be accomplished by the creation of a relatively higher curvature in the direction of the maximum energy. Secondly, the concept of minimum surface stiffness has to be considered in the particular case when the crystal prefers to grow in the direction where the surface has the smallest resistance to deformation.[85] At the end, the dendritic growth direction depends strongly on the anisotropy of the solid–liquid interfacial energy. In this respect, the Wulff construction can determine the anisotropy of the surface energy from small solid/liquid particles in equilibrium.[61]

2.4.2. Dynamics of the dendrite growth. The relationship between the growth conditions and the result of the microstructural features determines the dendrite growth dynamic. Specifically, for constrained growth (where solid structures grow under thermal gradients[86]) there is a relationship between tip dendrite radius and the growth rate. The dendritic growth models are usually based on diffusion-controlled transport in a parabolic solid–liquid interface. The scale of the microstructure is set by the competition between heat/solute diffusion and energy surface, where the basic model based on constant velocity solidification of a paraboloidal needle crystal is commonly used. Ivantsov,[87–89] provided the elementary mathematical treatment of the steady-state transport process at the solid/liquid interface by diffusion.

A steady state solution to the heat flow from a dendrite is provided by the Ivantsov equation for a paraboloid of revolution (3D):

$$\Delta = \mathrm{Pe}\exp((\mathrm{Pe})E_1\sqrt{\mathrm{Pe}}) \tag{2.25}$$

where $\Delta = c_p(T_f - T_\infty)/L_f$ is the dimensionless undercooling or solidification number which is the ratio of sensible heat to latent heat (also termed the Stefan number). Thus, T_f is the isothermal temperature and T_∞ the temperature far from equilibrium, E_1 is the exponential integral, c_p and L_f are the molar specific heat of the solid and the molar latent heat of fusion, respectively.

This solution uses a thermal diffusion equation as a boundary condition for the interface shape, expressing the thermal field in terms of Péclet Pe number:

$$\mathrm{Pe} = \frac{R_{tip}v^*}{2\alpha_l} \tag{2.26}$$

where R_{tip} is the radius of the tip growing at constant velocity v^* into an infinite undercooled melt with T_∞ constant, and α is the thermal diffusivity of the melt, which can be applied to the solid phase transformation of the product of reactants precursors using transition state theory.[90]

One of the limitations of Ivantsov relation is the surface energy, considering the surface isotropy, which does not satisfy the Gibbs–Thomson condition.[91] Therefore, it indicates the steady-state in the form of parabolic dendritic crystals. However, it cannot determine R_{tip} and v uniquely, it only determines the product of both. The temperature remains constant across the surface, which is far from the anisotropic interfacial energy situation.[77,92–94] Even the non-isothermal temperature boundary condition, for which the solution developed later by Horvay and Cahn[95] is relevant, does not satisfy the energy conservation and the non-isothermal equilibrium temperature boundary condition. Other approximations have been developed to overcome this limitation, based on the choice of a predetermined interface shape.[35,96] All these non-isothermal theories share the common feature that the values of v^* and R_{tip} can be determined independently, and they can be adapted to the determination of the dendritic shape for the solid transformation of perovskite films under rapid thermal growth.

3. Rapid perovskite crystallization

3.1. Crystallization kinetic

The crystallization kinetics for perovskite halide in a foreign substrate depend strongly on the interfacial energy of the solid/liquid interface. As well as to a lesser degree, the solid/gas interface, taking into account that most of the perovskite solidification processes are done in a controlled atmosphere.[97,98] Moreover, the chemical bonding particularities between surface and liquid defines the strength of cohesive molecular forces, thus competing with thermal diffusion to shape the final crystal growth.[99] Ayan A. Zhumekenov *et al.*[100] have investigated the role of the surface tension on perovskite crystallization, elucidating that the increase of surface tension leads to preferential nucleation at the surface layer, as shown in Fig. 4a. They establish a relationship between intramolecular forces, interfacial energy and crystal preferential growth. These fundamental studies are crucial for obtaining highly uniform films and high-performance large-scale devices; for instance, Yehao Deng *et al.*[101] have used amphoteric surfactants (L-α-phosphatidylcholine) to improve the adhesion of the perovskite to hydrophobic substrates, which allows them to scale-up the processes with fast blade-coating.

David P. McMeekin *et al.*[15] settled a relationship between the precursor solution's colloid concentration and the crystal

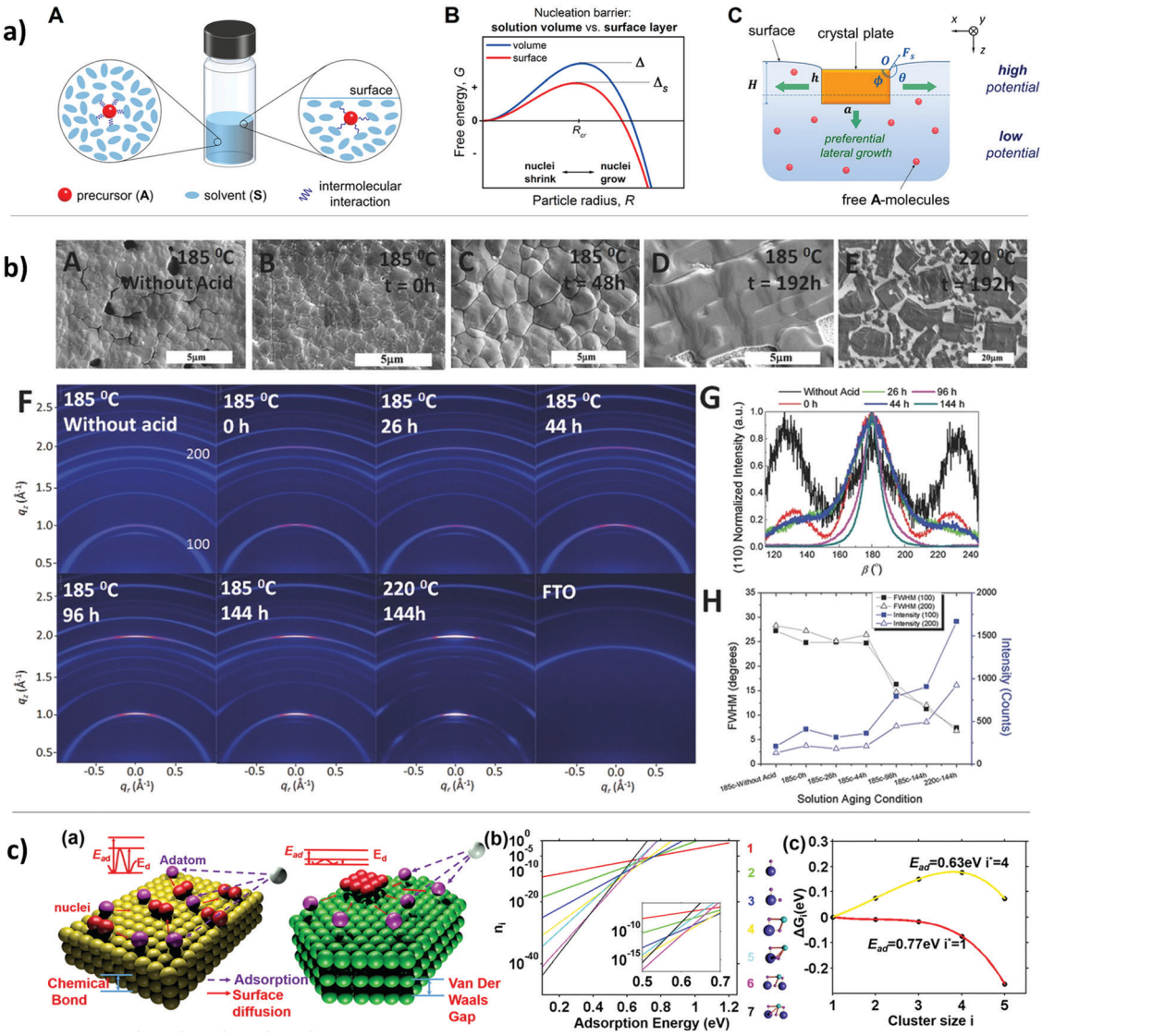

Fig. 4 (a) (A) Schematic of change in molecular interaction energies, (B) graph illustrating nucleation barriers for the solution surface and in the volume and (C) schematic of crystal growth during inverse temperature crystallization (reproduced with permission from ref. 98, ©2017 American Chemical Society). (b) Impact of colloids in the precursor solution on morphology and crystal quality. (A–E) Top-view SEM images of perovskite thin film with and without hydrohalic acids. (F) A series of 2D X-ray diffraction patterns. (G) Diffraction peak of corresponding perovskite thin film. (H) Full-width half maximum (FWHM) of (100) and (200) orientation corresponding to the (100) and (200) diffraction peaks (reproduced with permission from ref. 14, ©2017 The Authors. Published by Wiley-VCH Verlag GmbH & Co. KGaA, Weinheim). (c) (a) Schematic of different atomistic processes on substrate in terms of adsorption energy (E_{ad}), diffusion barrier (E_d), and nuclei sizes. (b) Plot of cluster coverage with a size i changes with E_{ad} (reproduced with permission from ref. 101, ©2015 American Chemical Society).

morphology of the perovskite thin film by adding hydrohalic, initiating the lead polyhalide colloids and acting as nucleation sites for further crystal growth, as can be seen in Fig. 4b. Additionally, they applied a solution aging time to control the size and dispersion of colloids in solution, thus increasing the grain size, crystallinity, and texture. In the same line, Benjamin J. Foley *et al.*[102] have demonstrated the use of additives for $MAPbI_3$ precursor solutions to alter the nucleation and growth processes. They were able to lower the free energy of the precursor by incorporating a sulfoxide, which strongly interacts with $MAPbI_3$ precursors, allowing a control over the nucleation density and growth rate. Yiping Wang *et al.*[103] showed how the bonding nature of 3D materials affects the kinetics of crystallization for extremely thin film growth, as can be seen in Fig. 4c. They proposed that weak van der Waals film-substrate interaction and low cohesive energy of the perovskite halide lead to 2D growth.

3.2. Antisolvent crystallization

In antisolvent (AS) crystallization, the solute crystallizes due to reduced solubility. AS occurs when exposing a solution to another solvent in which the product is almost insoluble. Additionally, the reduction of solubility can be performed by the gas flow on the crystallization process.[104–106] The way of reaching the supersaturation can determine several crystal features such as size, morphology, and coexisting atomic structures.[107] Nevertheless, this review focuses on liquid room temperature solvent cases. Although, a complete description of the crystallization process requires mass and energy balances.[108,109] In a continuous phase, the solute's mass balance contributes to the mass transfer into the growing crystal.[110]

There are many advantages in AS crystallization, such as low operating temperature and solvent activities that can have a deep effect in the polymorphic form of the final crystal growth.[111–113] Several models have been implemented for AS crystallization, in order to identify different patterns of behavior in terms of antisolvent addition rates, product average particle size and size distribution. Nowee *et al.*,[114] found that a growth rate relation results in sharper mean size increases in the feeding's early stages. Therefore, the population balance model, previously discussed in Sections 2.2.3 and 2.3.3, and the solution approach has been used for many authors to combine a nucleation and growth rate description for the AS crystallization.[115–117]

3.3. The antisolvent method for perovskite halide crystallization

The solution processability of perovskite materials is one of the most important advantages of PSCs.[118,119] The perovskite layer is typically deposited by a solution coating method.[14] A one-step spin-coating method is most often used because of its simplicity and low cost.[120–123] During the coating process, a so-called antisolvent is dropped on top of the layer for the perovskite crystal growth. Additional thermal annealing is necessary to remove the remaining solvent and reach a purer perovskite phase.[124–126] The solvent can be removed with AS and heat treatment, reaching the necessary driving force to induce crystallization on the perovskite films.[10] In the solution preparation methods, the humidity plays a fundamental role. It is well-known that perovskite $MAPbI_3$ films are sensitive to moisture, causing them to decompose into PbI_2.[11,12] Therefore, the manufacture of PSCs should be carried out under controlled atmosphere conditions with low humidity values.

In 2014 Nam Joong Jeon *et al.*[127] were the first to use the AS method for highly efficient perovskite solar cells. Starting from $MAPbI_2$ precursors in a mixture of DMSO/GBL solvents they used toluene to supersaturate and crystallize the thin film during spinning by applying a relatively low-temperature thermal treatment. In the same year 2014, Xiao *et al.*[128] used chlorobenzene as exhibiting a smooth and compact perovskite film surface, being composed of micron-sized grains as shown Fig. 5. In the Fig. 5, the transmission electron microscopy (TEM) image of the $CH_3NH_3PbI_3$ is a corroboration of the formation of a crystalline structure of the tetragonal CH3NH3PbI$_3$ phase, with the pattern of different thin film crystalline phases further confirmed by XRD analysis.

3.4. Acid–base reaction of perovskite halides

In 2016 Nayak *et al.*[129] proposed one of the first approaches for understanding the mechanism of perovskite halide crystallization from solution, as can be seen in Fig. 6a. In their observations, increasing the solution acidity can surpass the supersaturation state of the solutes and in turn decrease the strength of the solvent. This results in the onset of crystallization, which in turn can be decoupled from the changes of temperature. Therefore, the crystallization can be initiated by the change of the solvent and the acid–base equilibria in the solution. In order to achieve high quality perovskite films, Fei Zhang *et al.*[130] used a Lewis acid–base adduct approach as an effective way to control grain size, morphology and to suppress crystal defects.

Other approaches to control the rapid film growth have been carried out by Jin-Wook Lee *et al.*[131] as shown in Fig. 6b, which presents the Lewis acid reaction forming an adduct. In this work, different iodide compounds were dissolved in polar aprotic solvents acting as Lewis basis. DMSO was proven as an intermediate solvent for controlling $MAPbI_3$ morphology and grain size. $FAPbI_3$ perovskite composition found that thiourea was a better solvent-complement than DMSO because of the chemical interaction differences. Hamill *et al.*[132] demonstrated that solvent coordination with Pb_2^+ is correlated with Lewis basicity, which in turn influences solid-state perovskite formation, as shown in Fig. 6c. They focused on elucidating the role of Lewis basicity of the processing solvent, quantified by Gutmann's donor number, D_N, as a strong predictor of a solvent's ability to solvate perovskite precursors.

3.5. Role of common solvents for perovskite crystallization

3.5.1. Two-step deposition method. The choice of solvents used for the preparation of perovskite films is crucial as this profoundly influence on their formation due to Lewis acid–base interactions of the commonly used polar aprotic solvents with the perovskite precursors, especially PbI_2, as well as the formation of intermediate films. This in turn also fundamentally influences the quality of the obtained films and therefore device performance.

In the two-step approach for perovskite thin film preparation it is essential to ensure a complete reaction of the PbI_2 film

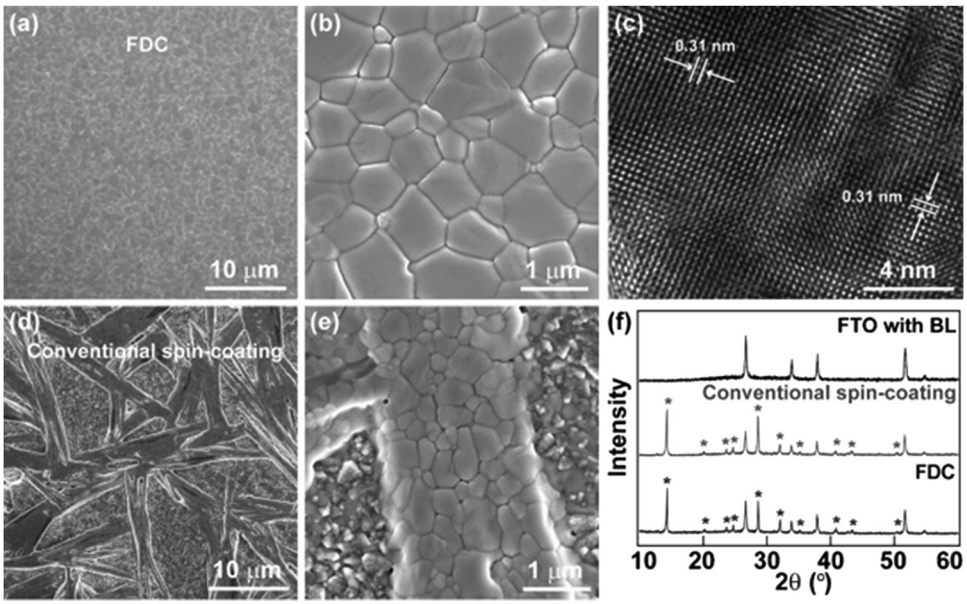

Fig. 5 Morphological and structural characterization of $MAPbI_3$ films prepared by fast crystallization-deposition (FDC) and a conventional spin-coating process (reproduced with permission from ref. 123, ©2014 Wiley-VCH Verlag GmbH & Co. KGaA, Weinheim).

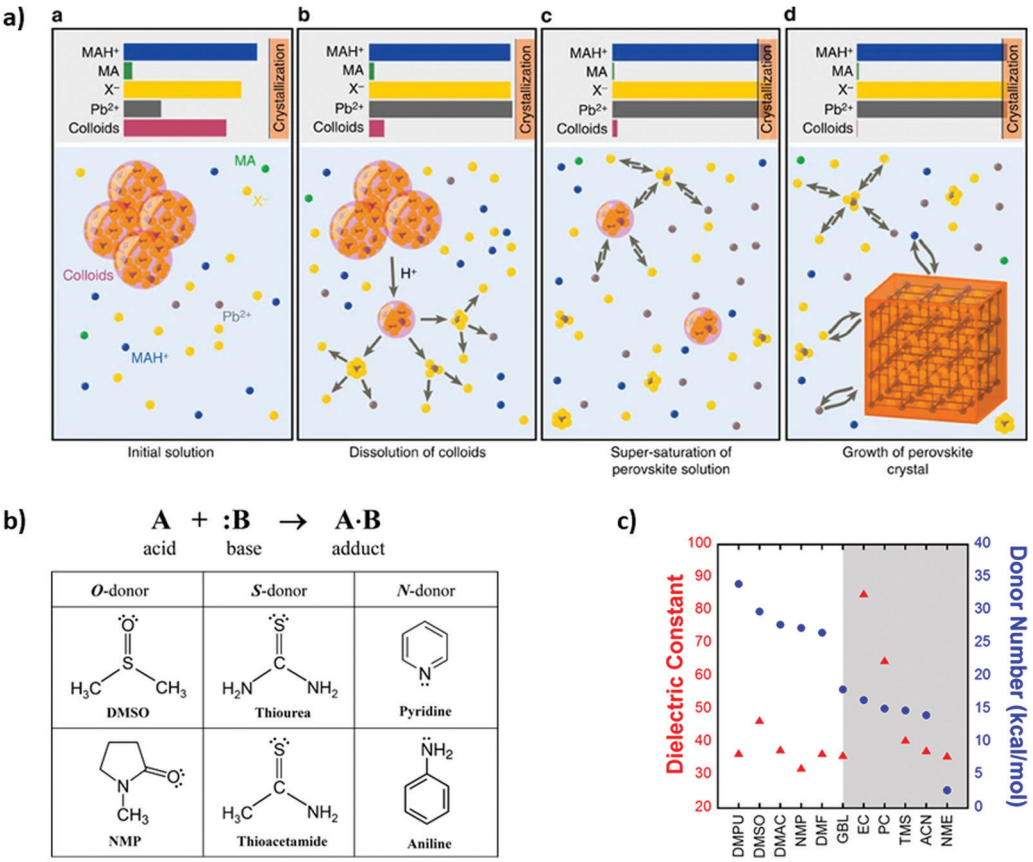

Fig. 6 (a) Schematic of the mechanism for crystallization of perovskite solid phase, where it represents the state of the system at several key points (reproduced with permission from ref. 124, ©2016 Springer Nature). (b) Representation of the Lewis acid (A)–base (B) reaction to form an adduct (A·B) with a dative bond and Lewis bases with different molecule donors (reproduced with permission from ref. 126, ©2016 American Chemical Society). (c) Dielectric constant (red triangles) and Gutmann's donor number (D_N, blue circles) of solvents used for perovskite processing (reproduced with permission from ref. 127, ©2017 American Chemical Society).

formed in the first step with the salt of the organic cation added in the second step as residual PbI_2 has been demonstrated to have detrimental effects on efficiency, reproducibility[133] and stability[133–135] of PSCs. This can be facilitated if mesoporous films of PbI_2 are formed in the first step allowing a more efficient conversion into the desired perovskite. Furthermore, this also prevents the formation of rough film surfaces otherwise caused by unit cell expansion upon intercalation of the organic halide.[136] Formation of mesoporous films can, for example, be achieved by controlling the nucleation/growth process during crystallization of PbI_2. To this end one can exploit the formation of $PbI_2{\cdot}x$Sol (Sol = solvent) films during spin-coating of a solution of PbI_2. Starting from a DMF solution of PbI_2 a $PbI_2{\cdot}x$DMF film forms with $x > 1$ due to the presence of unbound solvent in the fresh films.[136–139]

Upon thermal annealing a solvent-mediated Ostwald ripening process takes place leading to the formation of cracks and voids resulting in a mesoporous film.[140] However, due to the weak interaction of DMF with Pb^{2+} (D_N(DMF) = 26.6 kcal mol^{-1}) and its low boiling point (152 °C) DMF evaporates quickly not allowing enough time for this process. By keeping the $PbI_2{\cdot}x$DMF film in a closed Petri dish this time can be extended leading to the formation of larger voids and an increase in the fraction of voids in the whole film.[141] Alternatively, fast removal of DMF by applying drops of IPA (anti-solvent) onto the as-prepared $PbI_2{\cdot}x$DMF films can be employed to prepare mesoporous PbI_2.[139,142] In addition to using pure DMF the introduction of co-solvents and additives (*e.g.* DMSO, NMP, HMPA) with higher boiling points and improved interaction with PbI_2, as indicated by their higher D_Ns, has been used to improve the grain coarsening process during solvent annealing after spin-coating of PbI_2.[133,134,143–151] On the other hand, acetonitrile (D_N(MeCN) = 14.1 kcal mol^{-1}) as an example of a weakly Lewis basic solvent has also been used as an additive in PbI_2/DMF to improve grain morphology and roughness of the final perovskite film.[151,152]

In other instances, the $PbI_2{\cdot}x$Sol complexes formed before thermal annealing have been treated directly with the desired organic halide and shown to improve the final performance of PSCs.[153–156] This approach uses the intercalation of solvent molecules such as DMF, DMSO or NMP into the PbI_2 lattice to expand the PbI_2 unit cell along the *c*-axis[157] followed by an exchange with MAI or FAI to avoid unit cell expansion and therefore build-up of strain leading to rough surfaces during the perovskite formation step. The solvent molecules are removed during thermal annealing after the addition of the organic cation, inducing perovskite formation. More strongly coordinating solvents lead to larger grains in the final perovskite films.[156,157] This was explained by their stronger interaction with Pb^{2+} slowing down iodide coordination.[132,156,157]

Finally, in a study by Etgar *et al.*, the authors found that dropping toluene (AS) onto a perovskite precursor film prepared *via* the two-step method leads to a higher conductivity of the final film after subsequent thermal annealing. Furthermore, this treatment was found to efficiently suppress hysteresis. This demonstrates that the use of anti-solvents cannot only be used to control nucleation/growth kinetics and crystallinity of perovskite films but also to affect their electronic properties.

3.5.2. One-step deposition method. The judicious choice of solvents has also proven to be a valuable tool for optimizing perovskite thin film formation following the so-called one-step approach, where a common solution of PbX_2 and the halide salt of the desired organic cation is used to directly prepare the perovskite film in a single application by spin-coating. The most commonly used solvents for the preparation of this precursor solution include DMF, DMSO, GBL and NMP. This method traditionally suffers from incomplete surface coverage due to a slow rate of nucleation and fast growth of perovskite crystals leading to the formation of needle-like structures. Spiccia *et al.* demonstrated that this drawback could be circumvented by applying an anti-solvent (*e.g.* toluene, chlorobenzene) during the first seconds of spin-coating a solution of PbI_2 and MAI in DMF.[128] By doing so the solution quickly reaches a state of supersaturation due to the extraction of the precursor solvent by the anti-solvent leading to a burst of nucleation with newly formed nuclei covering the entire substrate. This is followed by a growth phase once the concentration has dropped below the critical value for nucleation at the end of which densely packed films displaying full substrate coverage are obtained.

A further level of control was introduced into this process by Sang Il Seok *et al.* who employed a "solvent engineering" approach to control perovskite film formation.[127] By spin-coating a solution of PbI_2, $PbBr_2$, MAI and MABr in a mixture of GBL and DMSO followed by toluene (anti-solvent) dripping they first obtained an intermediate phase film which was then converted into the final $MAPb(I_{1-x}Br_x)_3$ (x = 0.1–0.15) perovskite structure by thermal annealing. This led to the formation of highly uniform films with 100% surface coverage which could not be achieved when either DMSO was excluded from the precursor solution or no anti-solvent was applied during spin-coating. The intermediate phase which only formed in the presence of DMSO was suggested to contain MAI, PbI_2 and DMSO in a 1 : 1 : 1 ratio following a series of experiments excluding MABr and $PbBr_2$. Nam-Gyu Park and co-workers later prepared the clear intermediate phase from a precursor solution containing PbI_2, MAI and DMSO in an exact 1 : 1 : 1 ratio using diethyl ether as anti-solvent to avoid loss of DMSO due to their immiscibility.[158] The exact structure of the intermediate film was revealed by Yao *et al.* to consist of ribbons with the formula $[Pb_3I_8]^{2-}$ with MA^+ and DMSO molecules located in between to form a structure with the composition of $MA_2Pb_3I_8{\cdot}2$DMSO by using a 1 : 3 mixture of DMF and DMSO and toluene as anti-solvent.[158,159] The uncoordinated MAI was suggested to be either located on the surface of the intermediate phase crystals or homogeneously distributed around the intermediate phase domains.

The role of DMSO has been described as retarding the reaction between PbI_2 and MAI during evaporation of the solvent thereby granting more control over the crystallization process allowing the production of higher quality perovskite films. Interestingly, in a follow-up study optimizing the annealing conditions for conversion of $MA_2Pb_3I_8{\cdot}2$DMSO into $MAPbI_3$ perovskite the authors found that the devices demonstrating the highest PCEs of 15% still contained *ca.* 18% of the intermediate phase.[160]

They proposed that this prevented the formation of voids and cracks in the final perovskite film. Different ratios of PbI_2, MAI and DMSO have been explored to prepare devices with high efficiency and reproducibility.[160–162] Besides the commonly used anti-solvents toluene, diethyl ether and chlorobenzene also ethyl acetate,[163] trifluorotoluene,[163,164] hexane[165] (39) and a mixture of 6% IPA in chlorobenzene[165,166] have been shown to lead to high PCEs of final devices.

Using a mixture of NMP and DMA to dissolve PbI_2 and MAI Ding *et al.* developed a thermal annealing-free method for the preparation of high quality perovskite films presenting a PCE of 17.09% compared to marginally higher 17.38% including thermal annealing.[165–167] Padture *et al.* designed a solvent-solvent extraction method using diethyl ether to remove DMF after spin-coating their perovskite precursor solution in an effort to demonstrate a scalable way for the preparation of high-quality perovskite films.[168] This process was carried out at room temperature and required no further thermal annealing due to the low boiling point of diethyl ether. To address the issue of a narrow time window for immersing the film in the washing solvent, Zhu *et al.* added MACl to the perovskite precursor solution of PbI_2 and MAI in DMF/NMP to obtain a new ink which after blade coating gives a precursor film that remains stable for *ca.* 8 min during which it can be transferred into the diethyl ether bath.[168,169]

3.6. Perovskite film crystallization with IR pulses

3.6.1. Crystal nucleation & growth from solution. Some disadvantages of the AS crystallization approach are the additional costs associated with the high solvent consumption, difficult control of the growth rate, and the inherent solvent toxicity such as this of chlorinated compounds.[170,171] To avoid these problems, we have introduced the photonic pulse annealing for perovskite films, based on the acquired experiences of our home-developed FIRA (Flash InfraRed Annealing) method.[24] When a coated wet perovskite film is annealed, heat, provided by an IR pulse, is the driving force to reach the supersaturation state by rapidly decreasing the concentration, thereby initiating the nucleation and crystal growth. Looking at the specific FIRA case, crystal nucleation and growth can be controlled by three distinct parameters; the chamber temperature, the pulse duration and the pulse number, as shown in Fig. 7a. Once nucleation has occurred, it is followed by the growth of a crystalline phase. With respect to the perovskite crystal formation, it can involve numerous intermediate phases that can be determined by the growth rate.[30] The highly intense IR pulse causes the rapid evaporation of the solvent and provides the required thermal activation energy for crystal nucleation and growth.[33] Interestingly, the IR pulse heats the conductive contact, rapidly transferring the thermal energy through the solid/liquid interface, as shown in Fig. 7b, where the thermal diffusion and interfacial energy leads to crystal growth. Then, by adjusting the number of pulses the heating rate controls how supersaturation is reached and, as consequence, how the nuclei distribution from tiny clusters defines the final crystal shape.

The experimental investigation of crystal nucleation and growth is complex and still today a challenge for almost all systems. The classical nucleation theory stipulates that the critical nucleus is a sphere, where the important factor is how the total free energy associated with the formation of an average critical nucleus depends on its size, whatever the shape. However, this is a steady or quasi steady-state assumption. This analysis

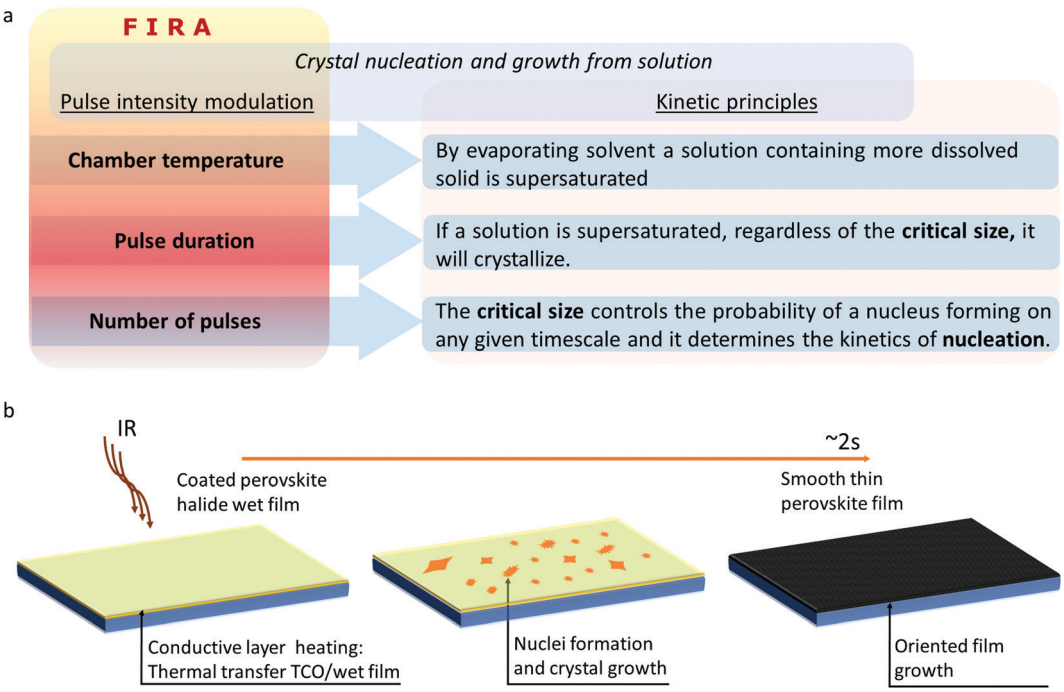

Fig. 7 Schematic of the kinetic process in the nucleation and growth of a crystalline perovskite film from a solution and (a) its relationship with the IR photonic pulses system, (b) the sequential thin film perovskite formation.

cannot be applicable to non-thermodynamic equilibrium as for example when the temperature changes too fast as in the case of the FIRA, which is still one of the main challenges for the rate calculations in these processes. Quasi-infinity steady-state numeric calculations corresponding to non-isothermal conditions, with a non-constant temperature rate, need to be performed.[172–174] Particularly in perovskite film processing, the calculation of nucleation and growth rates needs to be adapted for specific cases.

3.6.2. Crystallization dynamics. In a recent published work,[24] the authors describe the crystallization dynamics for the FIRA method. As shown in Fig. 8a and b, an *in situ* experiment was performed using a lower power output IR source and recording the crystallization of the coated film. A deposited $MAPbI_3$ wet film, under IR pulses, starts to nucleate, and growth occurs along energetically favorable crystallographic directions. The main observation for this experiment is how the dendritic growth is performed in a highly anisotropic medium, with thermal diffusion and interfacial energy as competing processes, as discussed in Section 2.4. Fig. 8c, shows a similar experience, but with an *ex situ* image recording and using FIRA (higher intense IR light) for the annealed films. Here, the film at 0.8 s evidences the formation of needle grains, at 1.4 and 2.4 seconds of a more compact dendritic structure, representative of the perovskite phases. The picture corresponding to 6.2 seconds shows a degraded film resulting from the evaporation of the MA^+ species, albeit containing remaining ions that can still form secondary phases. Note that, in the film annealed at 2.4 s, in contrast with the previous experience (Fig. 8a), the thermal diffusion overlaps the interfacial energy as a dominant effect, increasing the growth velocity of arms and tips and resulting in a more compact grain domain. Analogous to this experience, Ming He *et al.*,[175] have deposited micrometre-scale grain domains of perovskite films *via* convective flow and rapid solvent evaporation, promoting preferential crystal orientations at low temperatures and achieving high-performance PSCs.

3.6.3. Crystallization behavior of mixed perovskite solutions. Differences in chemical composition are in direct relationship with kinetic attachment and interfacial energy anisotropies. Different compositions need different pulse times so that the rate of nucleation is properly adjusted. Fig. 9a shows a temperature profile, and Fig. 9b SEM images for different perovskite chemical compositions annealed by IR pulses. The so-called pulsed-FIRA method,[27] with a number of extremely short pulses applied, has been used to control the nuclei distribution and crystal shape and size. In Fig. 9c, the resulting morphology differs in the films, *i.e.* for $MAPbI_3$ large and compact domains with internal dendritic structure can be observed. Mixing the bromide and iodide ($MAPbBr_{1.5}I_{1.5}$) leads to smaller domains. When cesium is mixed with MA ($CsMAPbBr_{1.5}I_{1.5}$) or MA is replaced by Cs ($CsPbBr_{1.5}I_{1.5}$), the crystal growth changes. Increasing the cesium and bromide concentration leads to smaller crystal domains. This arises from a change in the difference in chemical potential that drives crystal growth. As different precursors are added, the anisotropy varies. The driving force for dendrite growth requires some anisotropy, usually of the

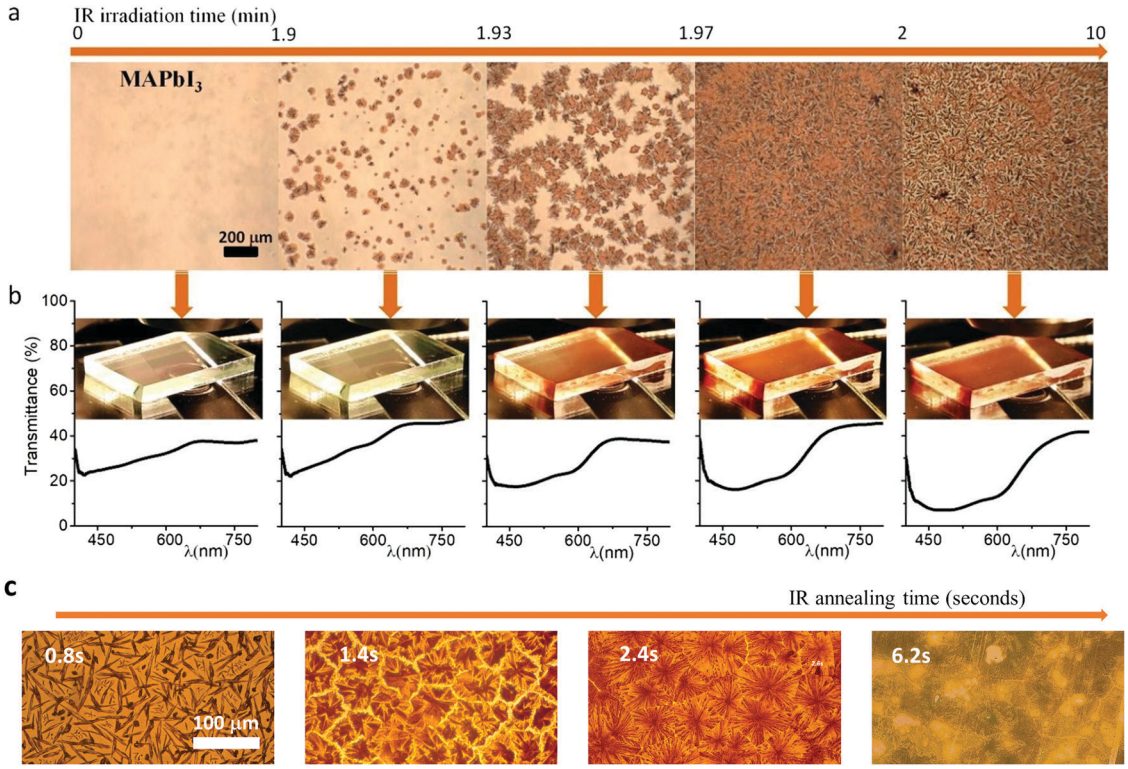

Fig. 8 (a) Optical images in transmittance mode of *in situ* perovskite crystallization from solution. (b) Transmittance spectra and images of the sample measured in (a). (c) Optical images taken in transmission mode for different flash times. (Reproduced with permission from ref. 23, ©2020, American Chemical Society).

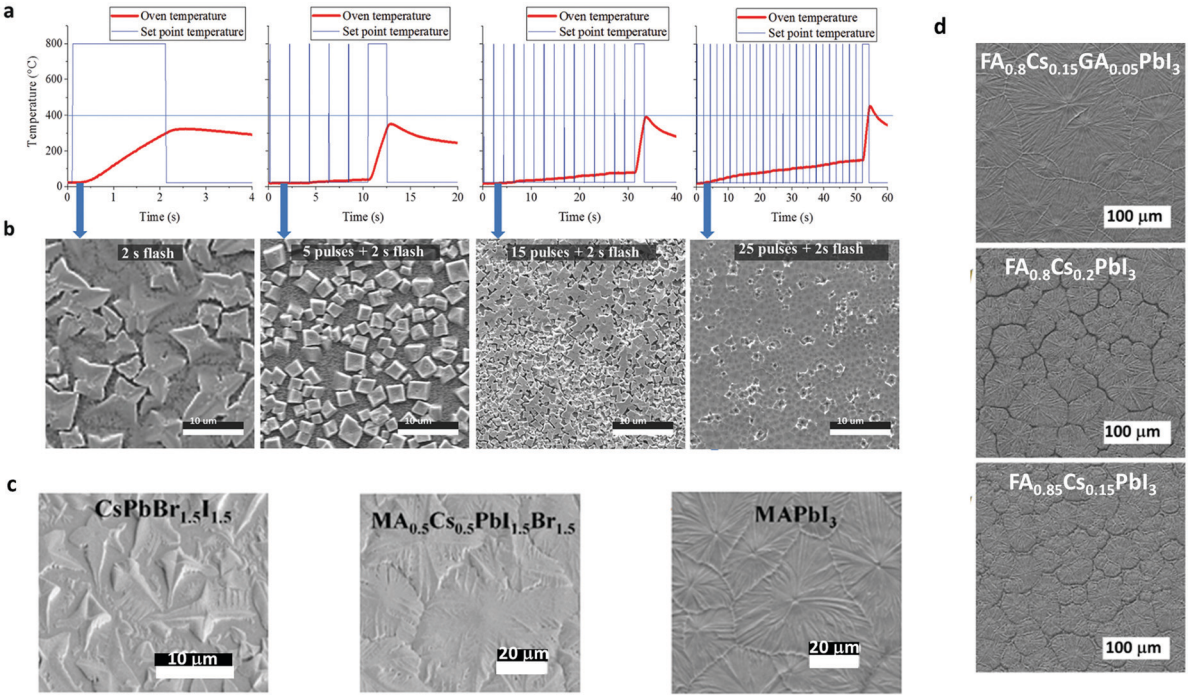

Fig. 9 (a) Temperature profile of the IR photonic pulses for inorganic perovskite and (b) the SEM images resulting from the annealed samples (adapted with permission from ref. 26, ©2018 Wiley-VCH Verlag GmbH & Co. KGaA, Weinheim). Top view SEM images of (c) three different perovskite chemical compositions and (d) three different stoichiometry for triple and double cation halide perovskites, all synthesized by a single IR pulse (adapted with permission from ref. 136, ©2019 The Author(s). Published by Elsevier Ltd[4]).

interfacial energy between crystal and solution/liquid, but that could also be anisotropy of the attachment kinetics for non-metallic systems.[176,177] If MA is replaced by Cs the crystal tends to grow in a more isotropic direction, forming faceted crystals without dendritic formations. In Fig. 9d-a slighter change of the perovskite triple cation composition on the grain boundary shape can be seen, allowing gaps in-between by playing with differences in kinetics according to the chemical structure of the precursors.[178]

4. Crystal grow and phase evolution

4.1. Crystal growth

The perovskite crystallization dynamics will depend on the processing method to be used, such as the commonly so-called one- and two-step depositions (as previously discussed in Section 3.3). This kind of "step deposition" methods are based on a solution process, and the number of steps depends on the solution precursor to be deposited.[122,179,180] All precursor can be contained in the same solutions, or different solutions with different solvents can be used, *i.e.* PbI_2 in DMSO and MAI in IPA. Diffusion processes play a fundamental role in the reaction process and crystallization. For instance, Tetsuhiko Miyadera *et al.*,[181] have observed anomalous diffusion, where the CH_3NH_3I diffuses into the PbI_2 films with fractal morphology, as shown in Fig. 9a. They claim that two growth orientation modes are possible, one which during the initial stage of the crystal reaction maintains the orientation of the initial materials and another, which represents the ordinary crystal orientation in the vertical direction; finally, we have the random orientation in the final stage of the crystal growth.

In terms of two steps deposition crystallization mechanism, Yongping Fu *et al.*[182] have proposed two growth mechanisms: a solid–liquid interfacial conversion reaction (Fig. 10b-a) and a dissolution–recrystallization growth mechanism (Fig. 10b-b). They argue that at a low MAI precursor concentration the conversion occurs by a solid–liquid interfacial reaction, and the perovskite phase is obtained by MAI diffusion into the layered PbI_2. Instead, Qiuju Liang *et al.*[181,183] have used a selective solvent annealing, a similar procedure to the antisolvent method. Here, the chosen solvent IPA promotes the precipitation and crystallization of lead halide, as shown in Fig. 10c, thus promoting the intercalation of MA^+ into an inorganic cage, resulting in a final perovskite phase. The Oswalt ripening process rearranges and coalesces during perovskite crystallization due to surface minimization, resulting in an increased crystal growth rate and optimized crystal orientation.

4.2. Temperature phase transition

The phase transition as a function of temperature in perovskite halide has been widely investigated.[7,184–186] However, there is still a lack of understanding how the temperature rate does affect the final perovskite grain shape and for instance the non-radiative defects on the solid films. In this effort, P. S. Whitfield *et al.*[187] have examined the crystal structures and structural phase lattice parameters and phase transitions of a $MAPbI_3$, Fig. 11a and b. They found that the cubic-tetragonal transition

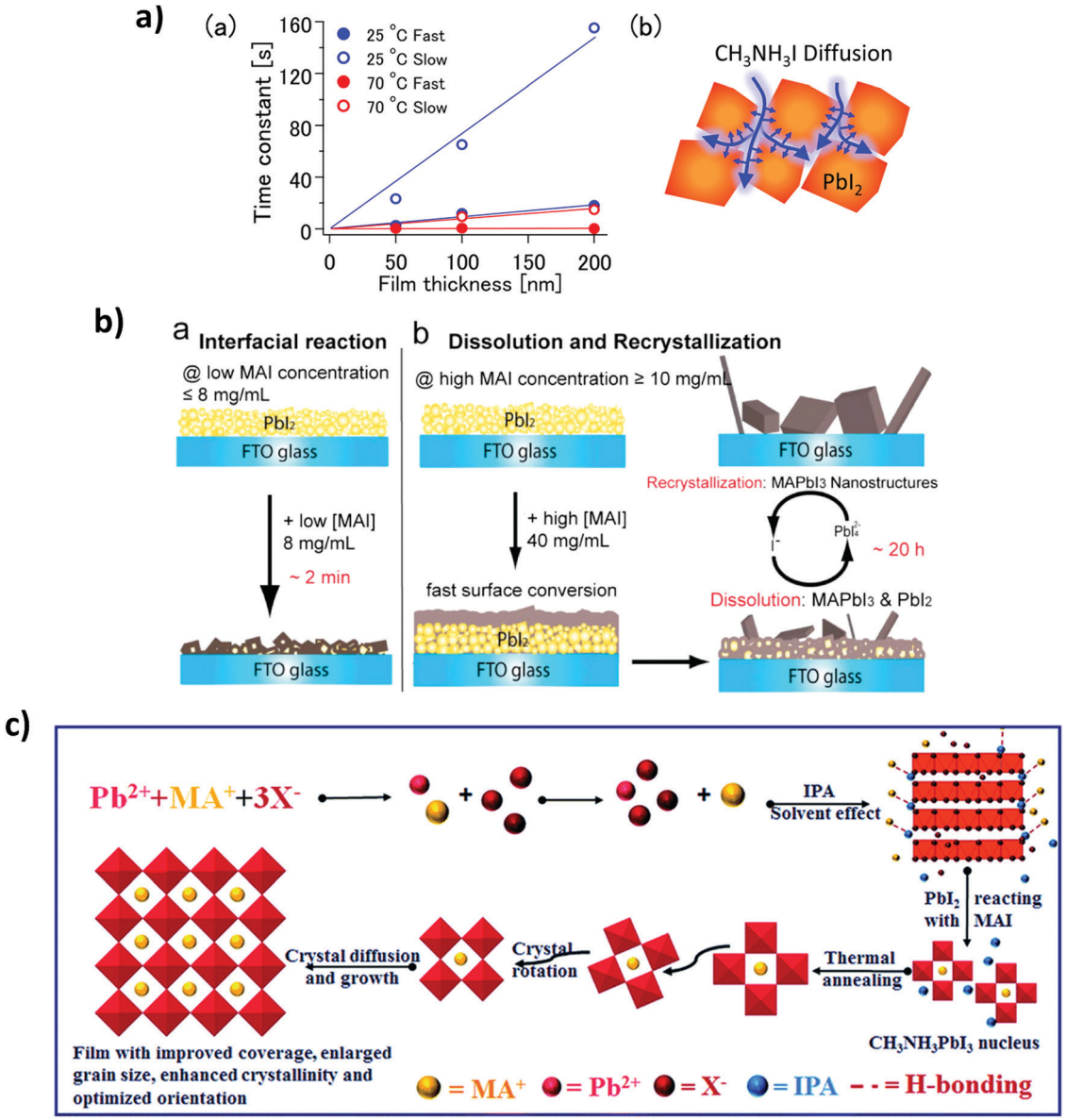

Fig. 10 (a) (a) Time constant values (τ) were obtained under various conditions fitting. (b) Schematic illustration of the MAPbI3 diffusion with fractal peculiarities (Reproduced with permission from ref. 139, ©2015, American Chemical Society). (b) Schematic illustrations of the two growth mechanisms of $MAPbI_3$ nanostructures, (a) interfacial reaction mechanism at lower MAI concentration and (b) dissolution–recrystallization growth mechanism at higher MAI concentration (reproduced with permission from ref. 140, ©2015, American Chemical Society). (c) The schematic diagram of the crystal nucleation during the selective solvent annealing and crystal growth during the thermal annealing processes (reproduced with permission of The Royal Society of Chemistry (RSC) on behalf of the Centre National de la Recherche Scientifique).

in $MAPbI_3$ is driven by an out-phase rotation mode, while the tetragonal-orthorhombic transition is primarily driven by an in-phase in $MAPbI_3$. They claimed that it is possible that the charge carrier scattering with these modes also contributes significantly to the electrical transport properties. Ilka M. Hermes *et al*,[188] have resolved an anisotropic distribution of carrier diffusion times on isolated $MAPbI_3$ grains correlated to the arrangement of ferroelastic twin domains, which reduces crystalline strain due to the cubic-tetragonal phase transition. Furthermore, Timothy W. Jones, *et al.*[189] have suggested that non-radiative defects come from local strains (at different scales), associated with inhomogeneous nucleation and growth, where local differences or intermediate phases during solution deposition would lead to heterogeneous growth.

The phase transition can also be elucidated from the rapid temperature profile, which allows us to identify the annealing parameters. In the first published study on the FIRA method,[26] the authors did comparative observations from a preliminary examination of the powder XRD data (Fig. 11c–a and b). While both perovskite films prepared, using the AS and FIRA-2.0 s methods exhibit similar XRD patterns, the 1.4 and 3.0 s FIRA annealed thin films show the boundary of the $MAPbI_3$ black

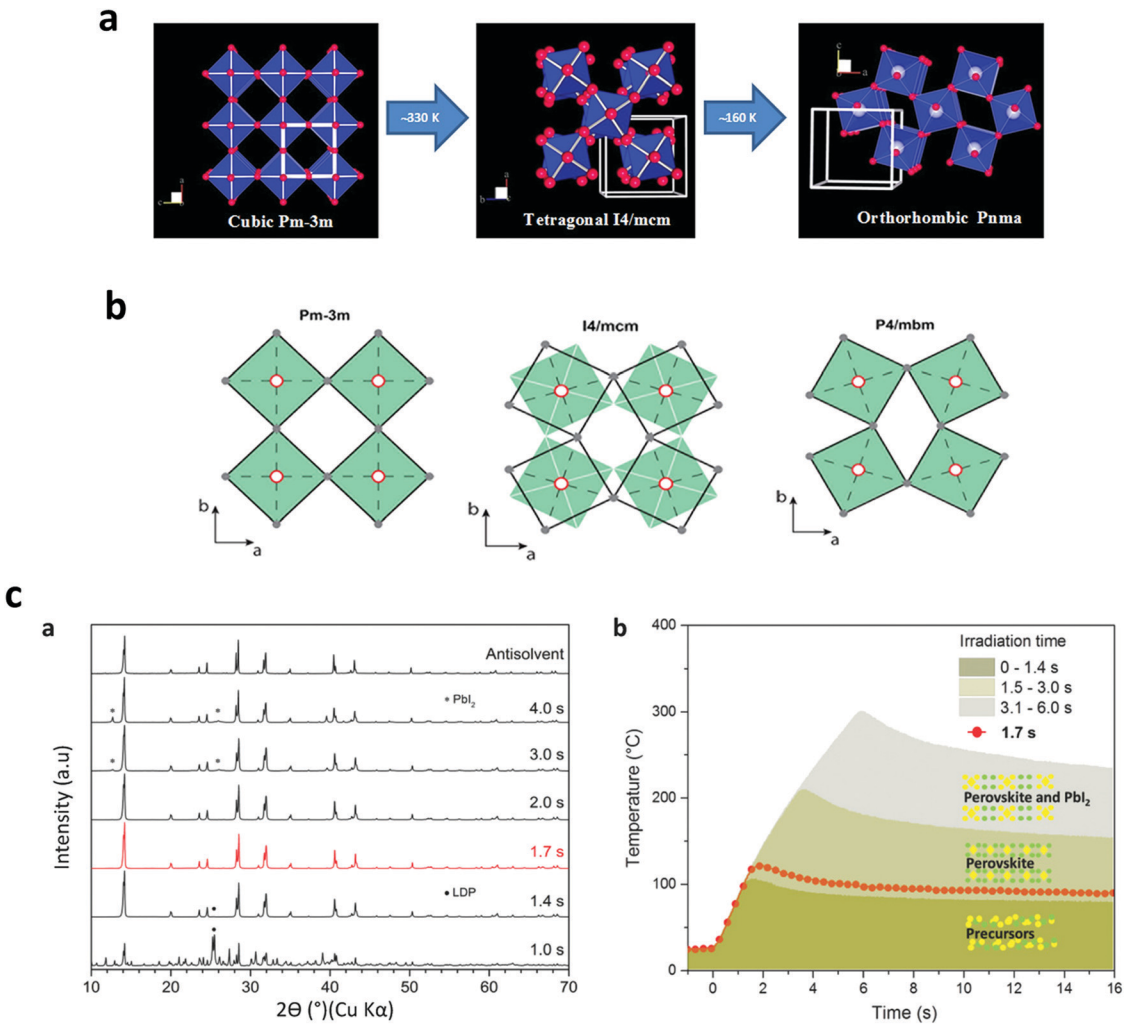

Fig. 11 (a) Cubic to tetragonal transition-rotational distortion mode, and tetragonal to orthorhombic transition-a combination of two different distortion modes. (b) Filled green squares and unfilled black squares displays the relative rotations of neighboring layers of PbI_6-octahedra along the *c* axis. (Reproduced with permission from ref. 145, ©2016, Springer Nature). (c) XRD patterns of $MAPbI_3$ powders (scrapped from synthesized films) (a) on FTO and (b) temperature profile of the perovskite phases, extracted from (a) (reproduced with permission from ref. 25, ©2019 American Chemical Society).

phase. FIRA can accurately determine phase evolution during annealing, as the short pulse duration allows screening of material properties at many different temperatures. Thus, making it possible to plot the temperature profile upon material degradation as a function of the annealing time, ~16 s, representative of the phase transition obtained from the XRD data. This phase diagram shows a close phase transition as is widely reported in literature,[190–192] and in turn is a useful tool for studying accurately the perovskite phase evolution under controlled and rapid thermal annealing.

4.3. Rapid thermal annealing

4.3.1. Thin film processing. It is well known that under rapid thermal treatment melted materials can preferentially grow in faceted and/or dendritic shapes.[193–195] For instance, in silicon solar cells, the control of the crystal-melt interface's morphology during oriented growth processes is critical to get high-quality crystals. In this practice, affecting the microstructures impacts the mechanical, optical, and electrical properties of materials.[196–198] The generation of crystal defects, such as dislocations and twin boundaries, is directly related to the crystal-melt interface's microstructure morphology.[199–201] According to Jackson's theory,[202] only Si{111} planes of the crystal-melt interfaces (facet planes) result in a smooth surface film. Other crystallographic planes result in a rough film surface, which means that the crystal growth rate can differ in crystallographic planes.

As well, it can be a consequence of the different interatomic distance in plane and the corresponding latent heat of phase transfer (and its relation with surface), where a complex interplay between geometric and electronic structure presents a challenge for theory.[203] The crystal rapid growth kinetics for melt can be extrapolated for solutions precursor materials, with similar primary consequences mainly in morphology and crystal shape. However, other complex phenomena arise for solution processes due to the interaction of the solvents and precursors as reactant materials.[204,205]

4.3.2. Microstructures and structural orientation. As discussed before, a perovskite wet film under rapid thermal annealing can grow in preferential directions and form microstructure arrangements. In the published work by Loreta Muscarrella *et al.*,[206] they used the FIRA method to grow the characteristic large $MAPbI_3$ crystal and to study its photophysical features. In Fig. 12a, it shows the XRD pattern for the two systems, AS and FIRA, deposited on ITO substrates. Both samples show a tetragonal XRD pattern but, in contrast, the FIRA sample shows a strong preferential orientation along the (112) and (400) planes (unit cell, Fig. 12a), according to the microstructural-arrangement. Fig. 12b and c shows a comparison from *the Kikuchi lines* obtained from the EBSD measurement. Citing the author: "*The AS sample (Fig. 12b) shows randomly oriented grains of hundreds of nanometers and on the contrary, in the FIRA sample (Fig. 11c), all grains are aligned along [100] and [112] directions (green and purple colors an along the z-axis Fig. 11d), and the two orientations are paired in larger regions, in agreement with XRD measurements*". The FIRA grains have smaller size on the nucleation centers of the "sunflower" formation" as shown in the EBDS and SEM images (Fig. 12e, f and g). The EBDS signal confirms the high order in the FIRA annealed perovskite films on planar electrodes as previously described by the XRD analysis. The rings conform to crystal microrods with a minimum length of around 5 μm (with increasing size from the nucleation centre to the ring border, reaching a maximum length of 20 μm).

4.3.3. Phase evolution: mechanisms & intermediate phases. A deep analysis of the phase evolution mechanisms for perovskite halide, specifically $MAPbI_3$ growth under rapid annealing (FIRA) was given by Xiao *et al.*[207] revealing the presence of two near-amorphous intermediate phases with local structures. By using pair distribution function analysis of X-ray total scattering data, the structure transformation from these intermediates occurs by the molecular cation insertion (with the required thermal activation) between the sheets of layered PbI_2 upon the crystallization of perovskites. As the schematic sequence presented in Fig. 13a–d shows, these intermediate phases adopt a 2D layered stacking arrangement, structurally related to the PbI_2 precursor and eventually transform into the 3D perovskite at high temperatures. The $[PbI_6]$ octahedra tilting is correlated with the reduced β-constant and the transformed layered building block to the final 3D perovskite phase. The $d(0\ 0\ 1)$ progressive change in R_xPbI_y modifies the interaction between the layered molecules and the $[PbI_6]$ sheet. As shown in Fig. 13d, the evolution of the *d*-spacing between the plane (001) in the intermediate phase almost matches the AS method with the 2 s FIRA, which establish clear evidence of a similar mechanism for phase transformation.[208,209]

The phase fraction (wt%) evolution and particle size of the components derived from the PDF refinement as a function of annealing time can be seen in Fig. 13f and g. The incorporation of MA layer during annealing tilts the PbI6 octahedra leading to conversion from intermediates phases (alpha and beta), the 2D building blocks, to form the 3D perovskite phase. In this study,

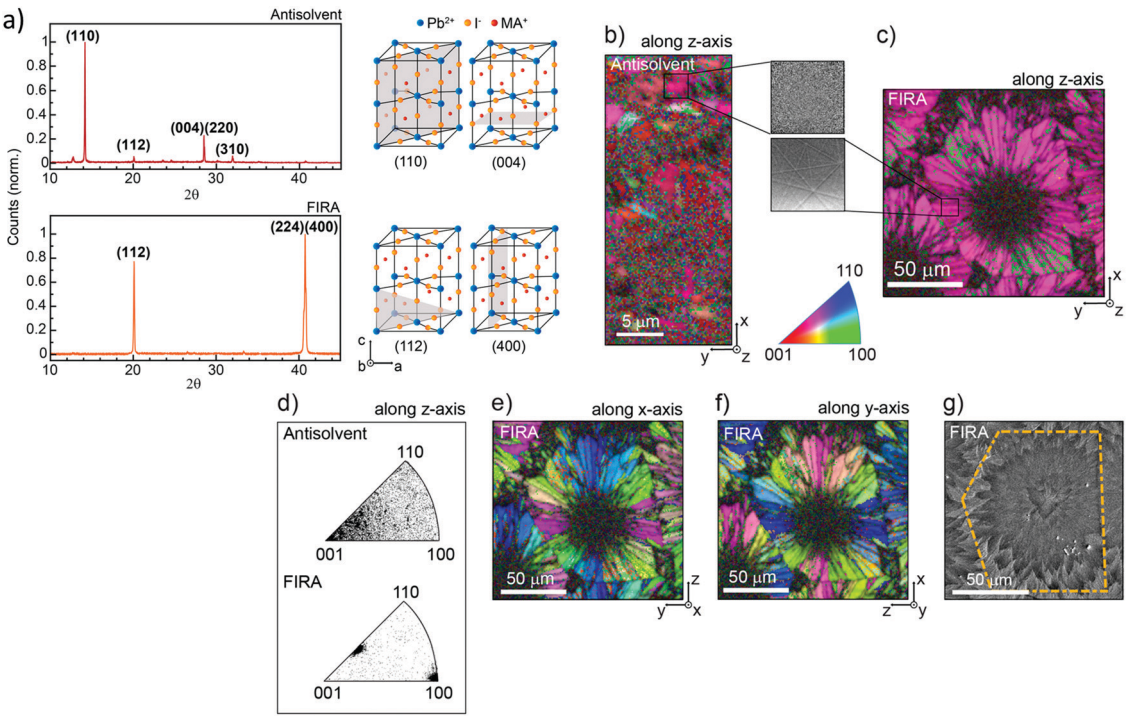

Fig. 12 (a) XRD patterns of AS and FIRA perovskite films with the corresponding unit cell cut in different planes. (b) Crystallographic orientation along the *z*-direction of the EBDS figure map. (Inset) Magnification of the Kikuchi patterns of the sample. (c) Zoom-out of the image. (d) Distribution of orientation for the two samples along the *z*-direction. (e) EBDS image of the FIRA sample showing the crystallographic orientation along the *x*-direction and (f) *y*-direction. (g) Crystallographic orientation along the *x*-direction and (f) *y*-direction shown in the FIRA sample's EBDS image. (g) SEM image confirming the grain size of the sample. (Reproduced with permission from ref. 162, ©2019 American Chemical Society).

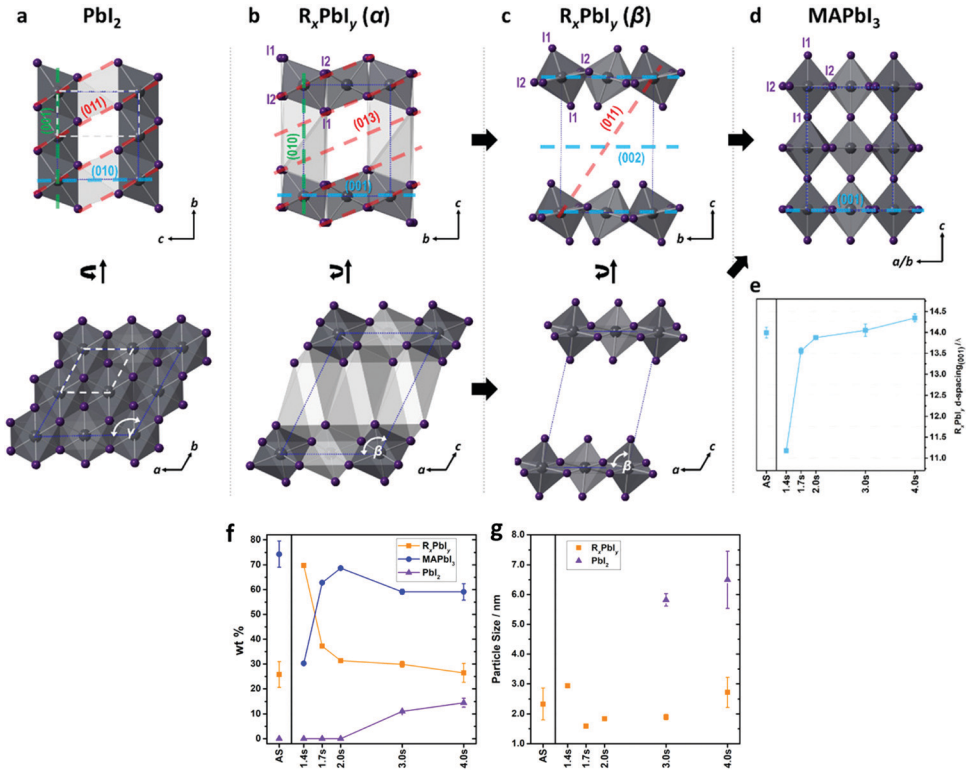

Fig. 13 PbI_6 structures of (a) PbI_2, (b) R_xPbI_y (α), (c) R_xPbI_y (β), and (d) $MAPbI_3$ viewed from different directions. (e) The evolution of the *d*-spacing between the (0 0 1) planes in R_xPbI_y. (f) Weight fraction evolution of each component and (g) particle sizes of PbI_2 and R_xPbI_y derived from PDF refinement. (Reproduced with permission from ref. 163, ©2019 American Chemical Society).

the 2.0 s of FIRA annealing give rise to 2D-to-3D structure transition reaching its maximum conversion rate. While intermediate phases contain around 30 wt%. The further increase of the temperature by continued exposure to IR (>2.0 s), results in a degradation of the thin film where both the intermediates and the perovskite decompose to PbI_2. Finally, changing the interfacial energy anisotropy by a bottom layer of mesoporous TiO_2 onto the FTO substrate does not significantly modify the perovskite phase evolution under the studied experimental conditions. However, there is a modification of the crystallization kinetics leading to different lateral domain sizes in the film, as predicted previously. Therefore, the thin film processing should avoid the formation of intermediate phases in order to enhance the stability and performance of PSCs.

5. Conclusions

In summary, the crystallization of perovskite films is one of the most important factors in order to manufacture highly efficient and stable devices. As discussed, there is a direct relationship between the quality of the solid film and efficiency losses and degradation. The target is to produce defect-tolerant thin films and low concentrations of non-radiant recombination centers and deep traps. Compositional engineering along with the deposition method are key instruments for perovskite crystal formation, which must be thoroughly understood before being chosen. The activation energy for the formation of perovskite crystals depends on the chemical reaction of the species involved and/or the temperature of the process. Together with the interfacial energy, specifically with the substrate to be used and the atmospheric conditions, it significantly influences crystal growth. Finally, in this review we reveal and relate the fundamentals of the FIRA manufacturing tool to be used as a reproducible method for highly crystalline perovskite thin film applications.

Conflicts of interest

There are no conflicts to declare.

References

1 A. Rajagopal, K. Yao and A. K.-Y. Jen, Toward Perovskite Solar Cell Commercialization: A Perspective and Research Roadmap Based on Interfacial Engineering, *Adv. Mater.*, 2018, **30**, 1800455.
2 Perovskite solar cells approaching commercialization, *Phys. Today*, 2014, DOI: 10.1063/pt.5.028283.
3 M. Jeong, *et al.*, Stable perovskite solar cells with efficiency exceeding 24.8% and 0.3 V voltage loss, *Science*, 2020, **369**, 1615–1620.
4 M. Pazoki, A. Hagfeldt and T. Edvinsson, *Characterization Techniques for Perovskite Solar Cell Materials*, Elsevier, 2019.
5 M. Graetzel, Molelcular Photovoltaics and Perovskite Solar Cells, Proceedings of the 10th International Conference on

Hybrid and Organic Photovoltaics, 2018, DOI: 10.29363/nanoge.hopv.2018.205.
6 J. L. Knutson, J. D. Martin and D. B. Mitzi, Tuning the band gap in hybrid tin iodide perovskite semiconductors using structural templating, *Inorg. Chem.*, 2005, **44**, 4699–4705.
7 N.-G. Park, M. Grätzel and T. Miyasaka, *Organic-Inorganic Halide Perovskite Photovoltaics: From Fundamentals to Device Architectures*, Springer, 2016.
8 N. S. Arul and V. D. Nithya, Revolution of Perovskite: Synthesis, Properties and Applications, *Springer Nature*, 2020.
9 K. Fu, A. W. Ho-Baillie, H. K. Mulmudi and P. T. T. Trang, *Perovskite Solar Cells: Technology and Practices*, CRC Press, 2019.
10 Electronic Traps and Their Correlations to Perovskite Solar Cell Performance *via* Compositional and Thermal Annealing Controls. 10.1021/acsami.8b17431.s001.
11 T. Miyasaka, Compositional engineering of cost efficient durable perovskite solar cells. Proceedings of the 3rd International Conference on Perovskite and Organic Photovoltaics and Optoelectronics, 2018, DOI: 10.29363/nanoge.iperop.2019.016.
12 W. Zhang, *Metal Halide Perovskite Crystals: Growth*, Techniques, Properties and Emerging Applications, MDPI, 2019.
13 *Interface-Dependent Radiative and Nonradiative Recombination in Perovskite Solar Cells*, DOI: 10.1021/acs.jpcc.8b00998.s001.
14 B. Chen, P. N. Rudd, S. Yang, Y. Yuan and J. Huang, Imperfections and their passivation in halide perovskite solar cells, *Chem. Soc. Rev.*, 2019, **48**, 3842–3867.
15 D. P. McMeekin, *et al.*, Crystallization Kinetics and Morphology Control of Formamidinium-Cesium Mixed-Cation Lead Mixed-Halide Perovskite *via* Tunability of the Colloidal Precursor Solution, *Adv. Mater.*, 2017, **29**, 1607039.
16 S. Zhang, *et al.*, Controlling Orientation Diversity of Mixed Ion Perovskites: Reduced Crystal Microstrain and Improved Structural Stability, *J. Phys. Chem. Lett.*, 2019, **10**, 2898–2903.
17 B. Chen, *et al.*, Synergistic Effect of Elevated Device Temperature and Excess Charge Carriers on the Rapid Light-Induced Degradation of Perovskite Solar Cells, *Adv. Mater.*, 2019, **31**, e1902413.
18 G. Tumen-Ulzii, *et al.*, Detrimental Effect of Unreacted PbI on the Long-Term Stability of Perovskite Solar Cells, *Adv. Mater.*, 2020, **32**, e1905035.
19 C. C. Boyd, R. Cheacharoen, T. Leijtens and M. D. McGehee, Understanding Degradation Mechanisms and Improving Stability of Perovskite Photovoltaics, *Chem. Rev.*, 2019, **119**, 3418–3451.
20 L. Liu, *et al.*, Grain-Boundary 'Patches' by In Situ Conversion to Enhance Perovskite Solar Cells Stability, *Adv. Mater.*, 2018, e1800544.
21 H. Lorenz, Solubility and Solution Equilibria in Crystallization, *Crystallization*, 2013, 35–74, DOI: 10.1002/9783527650323.ch3.
22 H. Esaka and W. Kurz, Columnar dendrite growth: Experiments on tip growth, *J. Cryst. Growth*, 1985, **72**, 578–584.
23 *Lithium Dendrite Growth Through Polymer Electrolytes*, ECS Meeting Abstracts (2013), DOI: 10.1149/ma2013-02/14/1097.
24 S. Sanchez, X. Hua and A. Guenzler, Flash infrared pulse time control of perovskite crystal nucleation and growth from solution, *Cryst. Growth Des.*, 2020, 670–679.
25 S. Sánchez, M. Vallés-Pelarda and J. A. Alberola-Borràs, Flash infrared annealing as a cost-effective and low environmental impact processing method for planar perovskite solar cells, *Mater. Today*, 2019, 39–46.
26 S. Sanchez, X. Hua, N. Phung and U. Steiner, Flash Infrared Annealing for Antisolvent-Free Highly Efficient Perovskite Solar Cells, *Adv. Energy*, 2018, **8**, 1702915.
27 S. Sanchez, N. Christoph and B. Grobety, Efficient and stable inorganic perovskite solar cells manufactured by pulsed flash infrared annealing, *Adv. Energy*, 2018, 1802060.
28 P. S. V. Ling, A. Hagfeldt and S. Sanchez, Flash Infrared Annealing for Perovskite Solar Cell Processing, *J. Vis. Exp.*, 2021, **168**, e61730, DOI: 10.3791/61730.
29 R. B. Fair, Junction Formation in Silicon by Rapid Thermal Annealing, *Rapid Therm. Process.*, 1993, 169–226, DOI: 10.1016/b978-0-12-247690-7.50009-3.
30 H. Gross, O. Khvostikova and U. Willkommen, Rapid Thermal Annealing for Large Area Applications. Society of Vacuum Coaters 57th (2014) Annual Technical Conference Proceedings (2015), DOI: 10.14332/svc14.proc.1825.
31 A. T. Fiory, Rapid Thermal Annealing, *Encyclopedia of Materials: Science and Technology*, 2001, pp. 8009–8017, DOI: 10.1016/b0-08-043152-6/01440-6.
32 C. Hill, S. Jones and D. Boys, Rapid Thermal Annealing - Theory and Practice, *Reduced Thermal Processing for ULSI*, 1989, 143–180, DOI: 10.1007/978-1-4613-0541-5_4.
33 H. L. Bhat, *Introduction to Crystal Growth: Principles and Practice*, CRC Press, 2014.
34 K. A. Jackson, *Kinetic Processes: Crystal Growth, Diffusion, and Phase Transitions in Materials*, John Wiley & Sons, 2010.
35 D. M. Herlach, *Solidification and Crystallization*, John Wiley & Sons, 2006.
36 K. Sangwal, *Nucleation and Crystal Growth: Metastability of Solutions and Melts*, John Wiley & Sons, 2018.
37 P. P. von Weimarn, 1879–1935. *Kolloid-Zeitschrift* **74** 1–10 (1936).
38 M. R. Leach, Lewis Acid–base Reaction Chemistry, 1999.
39 D. T. Haynie, Gibbs free energy – theory, *Biol. Thermodyn.*, 2012, 85–133, DOI: 10.1017/cbo9780511802690.005.
40 W. C. M. Lewis, A System of Physical Chemistry: Kinetic theory, 1918.
41 A. C. Lasaga, *Kinetic Theory in the Earth Sciences*, (2014), DOI: 10.1515/9781400864874.
42 A. E. S. Van Driessche, M. Kellermeier, L. G. Benning and D. Gebauer, *New Perspectives on Mineral Nucleation and Growth: From Solution Precursors to Solid Materials*, Springer, 2016.
43 Y. Shibuta, *et al.*, Heterogeneity in homogeneous nucleation from billion-atom molecular dynamics simulation of solidification of pure metal, *Nat. Commun.*, 2017, **8**, 10.
44 D. Bi, *et al.*, Polymer-templated nucleation and crystal growth of perovskite films for solar cells with efficiency greater than 21%, *Nat. Energy*, 2016, **1**, 16142.

45 F. L. Binsbergen, Natural and artificial heterogeneous nucleation in polymer crystallization, *J. Polym. Sci., Polym. Symp.*, 1977, **59**, 11–29.
46 M. K. Hoffmeyer, Heterogeneous Nucleation Catalysis and Grain Refinement, (1990).
47 A. Hulanicki, *Reactions of Acids and Bases in Analytical Chemistry*, Ellis Horwood, 1987.
48 K. A. Connors, Chemical Kinetics: The Study of Reaction Rates in Solution, Wiley-VCH Verlag GmbH, 1990.
49 A. C. Lasaga and D. M. Rye, Fluid flow and chemical reaction kinetics in metamorphic systems, *Am. J. Sci.*, 1993, **293**, 361–404.
50 S. Arrhenius, IV. Electrolytic dissociation versus hydration, *The London, Edinburgh, and Dublin Philosophical Magazine and Journal of Science*, 1889, **28**, 30–38.
51 J. W. Gooch, Arrhenius Equation. *Encyclopedic Dictionary of Polymers*, 2011, p. 48, DOI: 10.1007/978-1-4419-6247-8_800.
52 T. Turányi and A. S. Tomlin, *Analysis of Kinetic Reaction Mechanisms*, Springer, 2014.
53 J. W. P. Schmelzer, *Nucleation Theory and Applications*, John Wiley & Sons, 2006.
54 D. B. Abraham and C. M. Newman, Equilibrium Stranski–Krastanow and Volmer–Weber models, *EPL*, 2009, **86**, 16002.
55 M. Volmer, Thermodynamische Folgerungen ans der Zustandsgleichung für adsorbierte Stoffe, *Z. Phys. Chem.*, 1925, **115U**, 253–260.
56 R. McGraw, Arrhenius Temperature Dependence of Homogeneous Nucleation Rates, *Nucleation and Atmospheric Aerosols*, 2007, 144–148, DOI: 10.1007/978-1-4020-6475-3_29.
57 P. J. Phillips, Polymer Crystallization: Growth by Secondary Nucleation, *Encyclopedia of Materials: Science and Technology*, pp. 7253–7255 (2001), DOI: 10.1016/b0-08-043152-6/01290-0.
58 G. D. Botsaris, Secondary Nucleation – A Review, *Industrial Crystallization*, 1976, 3–22, DOI: 10.1007/978-1-4615-7258-9_1.
59 G. M. Maggioni and M. Mazzotti, A Stochastic Population Balance Equation Model for Nucleation and Growth of Crystals with Multiple Polymorphs, *Cryst. Growth Des.*, 2019, **19**, 4698–4709.
60 W. Sha and S. Malinov, The Johnson–Mehl–Avrami method: isothermal transformation kinetics, *Titanium Alloys*, 2009, 117–164, DOI: 10.1533/9781845695866.2.117.
61 J. A. Dantzig and M. Rappaz, *Solidification: 2nd Edition - Revised & Expanded*, EPFL Press, 2016.
62 A. D. Randolph and M. A. Larson, The Population Balance. *Theory of Particulate Processes*, 1971, pp. 41–63, DOI: 10.1016/b978-0-12-579650-7.50008-7.
63 H. A. Jakobsen, *The Population Balance Equation, Chemical Reactor Modeling*, 2014, pp. 807–865, DOI: 10.1007/978-3-540-68622-4_9.
64 M. A. Henson, *Distribution control of particulate systems based on population balance equation models*. Proceedings of the 2003 American Control Conference, 2003, DOI: 10.1109/acc.2003.1240456.
65 A. W. Vere, *Crystal Growth: Principles and Progress*, Springer Science & Business Media, 1988.
66 W. W. Mullins, Macroscopic description of interface migration by ledge and kink motion controlled by volume diffusion, *Metall. Trans. A*, 1991, **22**, 1225–1233.
67 D. Kondrashova and R. Valiullin, Freezing and Melting Transitions under Mesoscalic Confinement: Application of the Kossel–Stranski Crystal-Growth Model, *J. Phys. Chem. C*, 2015, **119**, 4312–4323.
68 C. Ratsch and A. Zangwill, Equilibrium theory of the Stranski–Krastanov epitaxial morphology, *Surf. Sci. Lett.*, 1993, **293**, A633.
69 W. K. Burton, N. Cabrera and F. C. Frank, Role of Dislocations in Crystal Growth, *Nature*, 1949, **163**, 398–399.
70 R. Bonnet, M. Loubradou and J. M. Pénisson, Burgers vector content of an interfacial ledge, *Phys. Rev. Lett.*, 1992, **69**, 104–107.
71 M. E. Gurtin, E. Fried and L. Anand, The Burgers vector and the flow of screw and edge dislocations in finite-deformation single-crystal plasticity, *J. Mech. Phys. Solids*, 2006, 588–592, DOI: 10.1017/cbo9780511762956.118.
72 V. A. Shneidman, Ostwald ripening with nucleation initial conditions, *AIP Conf. Proc.*, 2013, **1527**, 105–108, DOI: 10.1063/1.4803214.
73 C. I. Steefel and P. Van Cappellen, A new kinetic approach to modeling water-rock interaction: The role of nucleation, precursors, and Ostwald ripening, *Geochim. Cosmochim. Acta*, 1990, **54**, 2657–2677.
74 M. Koolyk, D. Amgar, S. Aharon and L. Etgar, Kinetics of cesium lead halide perovskite nanoparticle growth; focusing and de-focusing of size distribution, *Nanoscale*, 2016, **8**, 6403–6409.
75 N. D. Pham, *et al.*, Guanidinium thiocyanate selective Ostwald ripening induced large grain for high performance perovskite solar cells, *Nano Energy*, 2017, **41**, 476–487.
76 I. Steinbach, Effect of interface anisotropy on spacing selection in constrained dendrite growth, *Acta Mater.*, 2008, **56**, 4965–4971.
77 B. J. Spencer and H. E. Huppert, The relationship between dendrite tip characteristics and dendrite spacings in alloy directional solidification, *J. Cryst. Growth*, 1999, **200**, 287–296.
78 R. Dobrushin, R. Kotecký and S. Shlosman, Wulff Construction: A Global Shape from Local Interaction, *Translations of Mathematical Monographs* (1992), DOI: 10.1090/mmono/104.
79 E. Ringe, R. P. Van Duyne and L. D. Marks, Wulff Construction for Alloy Nanoparticles, *Nano Lett.*, 2011, **11**, 3399–3403.
80 G. D. Barmparis, Z. Lodziana, N. Lopez and I. N. Remediakis, Nanoparticle shapes by using Wulff constructions and first-principles calculations, *Beilstein J. Nanotechnol.*, 2015, **6**, 361–368.
81 H. M. Ding and L. C. Pu, Thermal Kinetics Phase Field Model for the Metals' Solidification - Mathematic Derivation of the Dendrite Growth Phase Field Variable Diffusion Model, *Appl. Mech. Mater.*, 2013, **364**, 614–618.
82 M. Hofacker and C. Miehe, A Phase Field Model for Three-Dimensional Dynamic Fracture and its Efficient Numerical Implementation, *PAMM*, 2011, **11**, 153–154.

83 M. Wouts, Surface Tension in the Dilute Ising Model. The Wulff Construction, *Commun. Math. Phys.*, 2009, **289**, 157–204.
84 Y. Lu, C. Beckermann and J. C. Ramirez, Three-dimensional phase-field simulations of the effect of convection on free dendritic growth, *J. Cryst. Growth*, 2005, **280**, 320–334.
85 J. P. van der Eerden, Relevance of surface roughening and surface melting for crystal growth, *J. Cryst. Growth*, 1993, **128**, 62–68.
86 G. Ding, W. Huang, X. Lin and Y. Zhou, Prediction of average spacing for constrained cellular/dendritic growth, *J. Cryst. Growth*, 1997, **177**, 281–288.
87 Z.-K. Liu and Y. Austin Chang, On the applicability of the Ivantsov growth equation, *J. Appl. Phys.*, 1997, **82**, 4838–4841.
88 T. Nishinaga, *Handbook of Crystal Growth: Fundamentals*, Elsevier, 2014.
89 G. Müller, J.-J. Métois and P. Rudolph, *Crystal Growth - From Fundamentals to Technology*, Elsevier, 2004.
90 B. C. Garrett and D. G. Truhlar, Transition State Theory, *Encyclopedia of Computational Chemistry*, 2002, DOI: 10.1002/0470845015.cta014.
91 A. Salhoumi and P. K. Galenko, Gibbs–Thomson condition for the rapidly moving interface in a binary system, *Phys. A*, 2016, **447**, 161–171.
92 W. Kurz and D. J. Fisher, Dendrite growth at the limit of stability: tip radius and spacing, *Acta Metall.*, 1981, **29**, 11–20.
93 S. Konstantinov, I. Smurov and G. Flamant, Influence of pulsed laser processing conditions on dendrite tip radius, *Appl. Surf. Sci.*, 1997, **109-110**, 113–123.
94 R. González-Cinca and L. Ramírez-Piscina, Numerical study of the shape and integral parameters of a dendrite, *Phys. Rev. E: Stat., Nonlinear, Soft Matter Phys.*, 2004, **70**, 051612.
95 G. Horvay and J. W. Cahn, Dendritic and spheroidal growth, *Acta Metall.*, 1961, **9**, 695–705.
96 S. G. R. Brown, T. Williams and J. A. Spittle, A cellular automaton model of the steady-state 'free' growth of a non-isothermal dendrite, *Acta Metall. Mater.*, 1994, **42**, 2893–2898.
97 Y. Sun, *et al.*, Engineering the Phases and Heterostructures of Ultrathin Hybrid Perovskite Nanosheets, *Adv. Mater.*, 2020, **32**, e2002392.
98 C. Bi, B. Chen, H. Wei, S. DeLuca and J. Huang, Efficient Flexible Solar Cell based on Composition-Tailored Hybrid Perovskite, *Adv. Mater.*, 2017, **29**, 1605900.
99 S. Cui, *et al.*, Rubidium Ions Enhanced Crystallinity for Ruddlesden-Popper Perovskites, *Adv. Sci.*, 2020, **7**, 2002445.
100 A. A. Zhumekenov, *et al.*, The Role of Surface Tension in the Crystallization of Metal Halide Perovskites, *ACS Energy Lett.*, 2017, **2**, 1782–1788.
101 Y. Deng, *et al.*, Surfactant-controlled ink drying enables high-speed deposition of perovskite films for efficient photovoltaic modules, *Nat. Energy*, 2018, **3**, 560–566.
102 B. J. Foley, *et al.*, Controlling nucleation, growth, and orientation of metal halide perovskite thin films with rationally selected additives, *J. Mater. Chem. A*, 2017, **5**, 113–123.
103 Y. Wang, Y. Shi, G. Xin, J. Lian and J. Shi, Two-Dimensional van der Waals Epitaxy Kinetics in a Three-Dimensional Perovskite Halide, *Cryst. Growth Des.*, 2015, **15**, 4741–4749.
104 D. J. Dixon and K. P. Johnston, Molecular thermodynamics of solubilities in gas antisolvent crystallization, *AIChE J.*, 1991, **37**, 1441–1449.
105 F. Kurniawansyah, L. Quachie, R. Mammucari and N. R. Foster, Improving the dissolution properties of curcumin using dense gas antisolvent technology, *Int. J. Pharm.*, 2017, **521**, 239–248.
106 R. Szostak, S. Sanchez and P. E. Marchezi, Revealing the Perovskite Film Formation Using the Gas Quenching Method by In Situ GIWAXS: Morphology, Properties, and Device Performance, *Adv. Funct. Mater.*, 2021, **31**, 2007473.
107 C. Zuo and L. Ding, An 80.11% FF record achieved for perovskite solar cells by using the NH4Cl additive, *Nanoscale*, 2014, **6**, 9935–9938.
108 J. Garside, Mass Crystallization, Number Balances and Size Distributions, *Sci. Technol. Cryst. Growth*, 1995, 209–220, DOI: 10.1007/978-94-011-0137-0_16.
109 M. Giulietti and A. Bernardo, Crystallization by Antisolvent Addition and Cooling, *Cryst. Sci. Technol.*, 2012, 380–395, DOI: 10.5772/50328.
110 K. Fukui and K. Maeda, Effects of crystal growth rate and heat and mass transfer on solute distribution, *Chem. Eng. Sci.*, 2002, **57**, 3133–3140.
111 A. Vanhook, Kinetics of Crystallization Growth of Crystals, *Crystallization*, 2013, 149–187, DOI: 10.1016/b978-1-4832-3051-1.50010-0.
112 S. Ueno, Y. Hamada and K. Sato, Controlling Polymorphic Crystallization ofn-Alkane Crystals in Emulsion Droplets through Interfacial Heterogeneous Nucleation, *Cryst. Growth Des.*, 2003, **3**, 935–939.
113 K. Liao, *et al.*, Aqueous solvent-regulated crystallization and interfacial modification in perovskite solar cells with enhanced stability and performance, *J. Power Sources*, 2020, **471**, 228447.
114 S. M. Nowee, S. Mostafa Nowee, A. Abbas and J. A. Romagnoli, Antisolvent crystallization: Model identification, experimental validation and dynamic simulation, *Chem. Eng. Sci.*, 2008, **63**, 5457–5467.
115 Z. K. Nagy, A population balance model approach for crystallization product engineering *via* distribution shaping control, *Comput.-Aided Chem. Eng.*, 2008, 139–144, DOI: 10.1016/s1570-7946(08)80028-4.
116 C. Y. Ma and X. Z. Wang, Model identification of crystal facet growth kinetics in morphological population balance modeling of l-glutamic acid crystallization and experimental validation, *Chem. Eng. Sci.*, 2012, **70**, 22–30.
117 Y. D. Shu, J. J. Liu, Y. Zhang and X. Z. Wang, A multi-stage multi-component transfer rate morphological population balance model for crystallization processes, *CrystEngComm*, 2019, **21**, 4212–4220.
118 L. Yang, *et al.*, Novel Insight into the Role of Chlorobenzene Antisolvent Engineering for Highly Efficient Perovskite Solar Cells: Gradient Diluted Chlorine Doping, *ACS Appl. Mater. Interfaces*, 2019, **11**, 792–801.

119 M. M. Tavakoli, *et al.*, Controllable Perovskite Crystallization *via* Antisolvent Technique Using Chloride Additives for Highly Efficient Planar Perovskite Solar Cells, *Adv. Energy Mater.*, 2019, **9**, 1803587.
120 *Unveiling the Concentration-Dependent Grain Growth of Perovskite Films from One- and Two-Step Deposition Methods: Implications for Photovoltaic Application*, DOI: 10.1021/acsami.7b05892.s001.
121 C. Liu, *et al.*, α-CsPbI Bilayers *via* One-Step Deposition for Efficient and Stable All-Inorganic Perovskite Solar Cells, *Adv. Mater.*, 2020, **32**, e2002632.
122 J.-H. Im, H.-S. Kim and N.-G. Park, Morphology-photovoltaic property correlation in perovskite solar cells: One-step versus two-step deposition of CH3NH3PbI3, *APL Mater.*, 2014, **2**, 081510.
123 F. Fang, J. Chen, G. Wu and H. Chen, Highly efficient perovskite solar cells fabricated by simplified one-step deposition method with non-halogenated anti-solvents, *Org. Electron.*, 2018, **59**, 330–336.
124 F. Yang, *et al.*, Enhanced Crystallization by Methanol Additive in Antisolvent for Achieving High-Quality MAPbI3 Perovskite Films in Humid Atmosphere, *ChemSusChem*, 2018, **11**, 2348–2357.
125 Y. Li, *et al.*, Acetic Acid Assisted Crystallization Strategy for High Efficiency and Long-Term Stable Perovskite Solar Cell, *Adv. Sci.*, 2020, **7**, 1903368.
126 D. Angmo, *et al.*, Controlling Homogenous Spherulitic Crystallization for High-Efficiency Planar Perovskite Solar Cells Fabricated under Ambient High-Humidity Conditions, *Small*, 2019, **15**, e1904422.
127 N. J. Jeon, *et al.*, Solvent engineering for high-performance inorganic-organic hybrid perovskite solar cells, *Nat. Mater.*, 2014, **13**, 897–903.
128 M. Xiao, *et al.*, A fast deposition-crystallization procedure for highly efficient lead iodide perovskite thin-film solar cells, *Angew. Chem., Int. Ed.*, 2014, **53**, 9898–9903.
129 P. K. Nayak, *et al.*, Mechanism for rapid growth of organic–inorganic halide perovskite crystals, *Nat. Commun.*, 2016, **7**, 13303.
130 F. Zhang, *et al.*, Suppressing defects through the synergistic effect of a Lewis base and a Lewis acid for highly efficient and stable perovskite solar cells, *Energy Environ. Sci.*, 2018, **11**, 3480–3490.
131 J.-W. Lee, H.-S. Kim and N.-G. Park, Lewis Acid–Base Adduct Approach for High Efficiency Perovskite Solar Cells, *Acc. Chem. Res.*, 2016, **49**, 311–319.
132 J. C. Hamill, J. Schwartz and Y.-L. Loo, Influence of Solvent Coordination on Hybrid Organic–Inorganic Perovskite Formation, *ACS Energy Lett.*, 2018, **3**, 92–97.
133 C. Jiang, S. L. Lim, W. P. Goh, F. X. Wei and J. Zhang, Improvement of $CH_3NH_3PbI_3$ Formation for Efficient and Better Reproducible Mesoscopic Perovskite Solar Cells, *ACS Appl. Mater. Interfaces*, 2015, **7**, 24726–24732.
134 H. Zhang, *et al.*, Nanostructures: A smooth CH3 NH3 PbI3 film *via* a new approach for forming the PbI2 nanostructure together with strategically high CH3 NH3 I concentration for high efficient planar-heterojunction solar cells, Adv. Energy mater. 23/2015, *Adv. Energy Mater.*, 2015, **5**, 1501354.
135 J. Cao, *et al.*, Porous PbI2 films for the fabrication of efficient, stable perovskite solar cells *via* sequential deposition, *J. Mater. Chem. A*, 2016, **4**, 10223–10230.
136 C.-H. Chiang and C.-G. Wu, Bulk heterojunction perovskite–PCBM solar cells with high fill factor, *Nat. Photonics*, 2016, **10**, 196–200.
137 H. Zheng, W. Wang, S. Yang, Y. Liu and J. Sun, A facile way to prepare nanoporous PbI2 films and their application in fast conversion to CH3NH3PbI3, *RSC Adv.*, 2016, **6**, 1611–1617.
138 X. B. Cao, *et al.*, High quality perovskite films fabricated from Lewis acid–base adduct through molecular exchange, *RSC Adv.*, 2016, **6**, 70925–70931.
139 A. Wakamiya, *et al.*, Reproducible fabrication of efficient perovskite-based solar cells: X-ray crystallographic studies on the formation of CH3NH3PbI3 layers, *Chem. Lett.*, 2014, **43**, 711–713.
140 X. Cao, *et al.*, Elucidating the Key Role of a Lewis Base Solvent in the Formation of Perovskite Films Fabricated from the Lewis Adduct Approach, *ACS Appl. Mater. Interfaces*, 2017, **9**, 32868–32875.
141 T. Liu, *et al.*, Mesoporous PbI2 Scaffold for High-Performance Planar Heterojunction Perovskite Solar Cells, *Adv. Energy Mater.*, 2016, **6**, 1501890.
142 W.-T. Wang, S. K. Das and Y. Tai, Fully Ambient-Processed Perovskite Film for Perovskite Solar Cells: Effect of Solvent Polarity on Lead Iodide, *ACS Appl. Mater. Interfaces*, 2017, **9**, 10743–10751.
143 J. Cao, *et al.*, Identifying the Molecular Structures of Intermediates for Optimizing the Fabrication of High-Quality Perovskite Films, *J. Am. Chem. Soc.*, 2016, **138**, 9919–9926.
144 C. Yi, X. Li, J. Luo, S. M. Zakeeruddin and M. Grätzel, Perovskite Photovoltaics with Outstanding Performance Produced by Chemical Conversion of Bilayer Mesostructured Lead Halide/TiO2 Films, *Adv. Mater.*, 2016, **28**, 2964–2970.
145 W. Wu, *et al.*, Tuning PbI2 layers by *n*-butanol additive for improving CH3NH3PbI3 light harvesters of perovskite solar cells, *RSC Adv.*, 2016, **6**, 89609–89613.
146 X. Cao, *et al.*, Control of the morphology of PbI2 films for efficient perovskite solar cells by strong Lewis base additives, *J. Mater. Chem. C*, 2017, **5**, 7458–7464.
147 Y. Shi, *et al.*, Effects of 4-tert-butylpyridine on perovskite formation and performance of solution-processed perovskite solar cells, *J. Mater. Chem. A*, 2015, **3**, 22191–22198.
148 K. Sun, *et al.*, Lewis acid–base interaction-induced porous PbI2 film for efficient planar perovskite solar cells, *ACS Appl. Energy Mater*, 2018, **1**, 2114–2122.
149 B. Li, *et al.*, Facile deposition of mesoporous PbI2 through DMF:DMSO solvent engineering for sequentially deposited metal Halide perovskites, *ACS Appl. Energy Mater*, 2020, **3**, 3358–3368.
150 Z.-W. Kwang, C.-W. Chang, T.-Y. Hsieh, T.-C. Wei and S.-Y. Lu, Solvent-modulated reaction between mesoporous PbI2 film and CH3NH3I for enhancement of photovoltaic

performances of perovskite solar cells, *Electrochim. Acta*, 2018, **266**, 118–129.
151 P. M. Moreno-Romero, *et al.*, Roughness and structural modification of PbI2 thin films by isopropanol treatment to improve methylammonium lead halide formation and solar cell efficiency, *J. Mater. Sci.: Mater. Electron.*, 2019, **30**, 17491–17503.
152 L. Li, *et al.*, The Additive Coordination Effect on Hybrids Perovskite Crystallization and High-Performance Solar Cell, *Adv. Mater.*, 2016, **28**, 9862–9868.
153 W. S. Yang, *et al.*, Solar Cells. High-performance photovoltaic perovskite layers fabricated through intramolecular exchange, *Science*, 2015, **348**, 1234–1237.
154 L. Zhi, *et al.*, Perovskite Solar Cells Fabricated by Using an Environmental Friendly Aprotic Polar Additive of 1,3-Dimethyl-2-imidazolidinone, *Nanoscale Res. Lett.*, 2017, **12**, 632.
155 Y. Jo, *et al.*, High performance of planar perovskite solar cells produced from PbI2(DMSO) and PbI2(NMP) complexes by intramolecular exchange, *Adv. Mater. Interfaces*, 2016, **3**, 1500768.
156 X. B. Cao, *et al.*, Fabrication of high quality perovskite films by modulating the Pb–O bonds in Lewis acid–base adducts, *J. Mater. Chem. A*, 2017, **5**, 8416–8422.
157 C. C. Coleman, H. Goldwhite and W. Tikkanen, A review of intercalation in heavy metal iodides, *Chem. Mater.*, 1998, **10**, 2794–2800.
158 N. Ahn, *et al.*, Highly Reproducible Perovskite Solar Cells with Average Efficiency of 18.3% and Best Efficiency of 19.7% Fabricated *via* Lewis Base Adduct of Lead(II) Iodide, *J. Am. Chem. Soc.*, 2015, **137**, 8696–8699.
159 Y. Rong, *et al.*, Solvent engineering towards controlled grain growth in perovskite planar heterojunction solar cells, *Nanoscale*, 2015, **7**, 10595–10599.
160 Y. Rong, *et al.*, Critical kinetic control of non-stoichiometric intermediate phase transformation for efficient perovskite solar cells, *Nanoscale*, 2016, **8**, 12892–12899.
161 Y. Bai, *et al.*, A pure and stable intermediate phase is key to growing aligned and vertically monolithic perovskite crystals for efficient PIN planar perovskite solar cells with high processibility and stability, *Nano Energy*, 2017, **34**, 58–68.
162 Y. Wang, *et al.*, Interfacial modification towards highly efficient and stable perovskite solar cells, *Nanoscale*, 2020, **12**, 18563–18575.
163 P. Zhou, *et al.*, Efficient and stable mixed perovskite solar cells using P3HT as a hole transporting layer, *J. Mater. Chem. C*, 2018, **6**, 5733–5737.
164 S. Paek, *et al.*, From nano- to micrometer scale: The role of antisolvent treatment on high performance perovskite solar cells, *Chem. Mater.*, 2017, **29**, 3490–3498.
165 Y. Yu, *et al.*, Ultrasmooth Perovskite Film *via* Mixed Anti-Solvent Strategy with Improved Efficiency, *ACS Appl. Mater. Interfaces*, 2017, **9**, 3667–3676.
166 Y. Wang, *et al.*, Stitching triple cation perovskite by a mixed anti-solvent process for high performance perovskite solar cells, *Nano Energy*, 2017, **39**, 616–625.
167 X. Fang, *et al.*, Annealing-free perovskite films based on solvent engineering for efficient solar cells, *J. Mater. Chem. C*, 2017, **5**, 842–847.
168 Y. Zhou, *et al.*, Room-temperature crystallization of hybrid-perovskite thin films *via* solvent–solvent extraction for high-performance solar cells, *J. Mater. Chem. A*, 2015, **3**, 8178–8184.
169 M. Yang, *et al.*, Perovskite ink with wide processing window for scalable high-efficiency solar cells, *Nat. Energy*, 2017, **2**, 17038.
170 High-Power and Flexible Indoor Solar Cells *via* Controlled Growth of Perovskite Using a Greener Antisolvent, DOI: 10.1021/acsaem.0c00997.s003.
171 Y. Wang, T. Mahmoudi, W.-Y. Rho and Y.-B. Hahn, Fully-ambient-air and antisolvent-free-processed stable perovskite solar cells with perovskite-based composites and interface engineering, *Nano Energy*, 2019, **64**, 103964.
172 R. J. Schaefer, The validity of steady-state dendrite growth models, *J. Cryst. Growth*, 1978, **43**, 17–20.
173 D. A. Kessler and H. Levine, Computational approach to steady-state eutectic growth, *J. Cryst. Growth*, 1989, **94**, 871–879.
174 S. Epure, T. Duffar and L. Braescu, Comparison between analytical and numeric determination of the interface curvature during dewetted Bridgman crystal growth, *J. Cryst. Growth*, 2008, **310**, 1559–1563.
175 M. He, *et al.*, Meniscus-assisted solution printing of large-grained perovskite films for high-efficiency solar cells, *Nat. Commun.*, 2017, **8**, 16045.
176 M. Rappaz and W. Kurz, Dendrites solidified by computer, *Nature*, 1995, **375**, 103.
177 T. Haxhimali, A. Karma, F. Gonzales and M. Rappaz, Orientation selection in dendritic evolution, *Nat. Mater.*, 2006, **5**, 660–664.
178 S. Sánchez, J. Jerónimo-Rendon, M. Saliba and A. Hagfeldt, Highly efficient and rapid manufactured perovskite solar cells *via* Flash InfraRed Annealing, *Mater. Today*, 2020, **35**, 9–15.
179 G. Cotella, *et al.*, One-step deposition by slot-die coating of mixed lead halide perovskite for photovoltaic applications, *Sol. Energy Mater. Sol. Cells*, 2017, **159**, 362–369.
180 H.-S. Ko, J.-W. Lee and N.-G. Park, 15.76% efficiency perovskite solar cells prepared under high relative humidity: importance of PbI2 morphology in two-step deposition of CH3NH3PbI3, *J. Mater. Chem. A*, 2015, **3**, 8808–8815.
181 T. Miyadera, *et al.*, Crystallization Dynamics of Organolead Halide Perovskite by Real-Time X-ray Diffraction, *Nano Lett.*, 2015, **15**, 5630–5634.
182 Y. Fu, *et al.*, Solution growth of single crystal methylammonium lead halide perovskite nanostructures for optoelectronic and photovoltaic applications, *J. Am. Chem. Soc.*, 2015, **137**, 5810–5818.
183 Q. Liang, *et al.*, Enhancing the crystallization and optimizing the orientation of perovskite films *via* controlling nucleation dynamics, *J. Mater. Chem. A*, 2016, **4**, 223–232.
184 A. Dobrovolsky, A. Merdasa, E. L. Unger, A. Yartsev and I. G. Scheblykin, Defect-induced local variation of crystal phase transition temperature in metal-halide perovskites, *Nat. Commun.*, 2017, **8**, 34.

185 *Local Rearrangement of the Iodide Defect Structure Determines the Phase Segregation Effect in Mixed-Halide Perovskites*, DOI: 10.1021/acs.jpclett.0c01127.s001.
186 J. Lin, *et al.*, Thermochromic halide perovskite solar cells, *Nat. Mater.*, 2018, **17**, 261–267.
187 P. S. Whitfield, *et al.*, Corrigendum: Structures, Phase Transitions and Tricritical Behavior of the Hybrid Perovskite Methyl Ammonium Lead Iodide, *Sci. Rep.*, 2017, **7**, 42831.
188 I. M. Hermes, *et al.*, Anisotropic carrier diffusion in single MAPbI3 grains correlates to their twin domains, *Energy Environ. Sci.*, 2020, **13**, 4168–4177, DOI: 10.1039/d0ee01016b.
189 T. W. Jones, *et al.*, Lattice strain causes non-radiative losses in halide perovskites, *Energy Environ. Sci.*, 2019, **12**, 596–606.
190 A. Baumann, *et al.*, Identification of Trap States in Perovskite Solar Cells, *J. Phys. Chem. Lett.*, 2015, **6**, 2350–2354.
191 T. Wang, *et al.*, Indirect to direct bandgap transition in methylammonium lead halide perovskite, *Energy Environ. Sci.*, 2017, **10**, 509–515.
192 J. M. Frost, K. T. Butler and A. Walsh, Molecular ferroelectric contributions to anomalous hysteresis in hybrid perovskite solar cells, *APL Mater.*, 2014, **2**, 081506.
193 L. Pfeiffer, S. Paine, G. H. Gilmer, W. van Saarloos and K. W. West, Pattern Formation Resulting from Faceted Growth in Zone-Melted Thin Films, *Phys. Rev. Lett.*, 1985, **54**, 1944–1947.
194 J. Johansson, B. A. Wacaser, K. A. Dick and W. Seifert, Growth related aspects of epitaxial nanowires, *Nanotechnology*, 2006, **17**, S355–S361.
195 D. P. Woodruff and D. P. Woodruff, *The Solid–Liquid Interface*, CUP Archive, 1973.
196 H. M. Anderson and P. J. Hargis, A Model for Silicon Dendrite Growth During Laser/Plasma Deposition from a Silane Discharge, *MRS Proc.*, 1986, **75**, 755–764.
197 G. Y. Chen, H. K. Lin and C. W. Lan, Phase-field modeling of twin-related faceted dendrite growth of silicon, *Acta Mater.*, 2016, **115**, 324–332.
198 T. Aoyama, Y. Takamura and K. Kuribayashi, Dendrite growth processes of silicon and germanium from highly undercooled melts, *Metall. Mater. Trans. A*, 1999, **30**, 1333–1339.
199 B.-C. Sim, Y.-H. Jung, J.-E. Lee and H.-W. Lee, Effect of the crystal–melt interface on the grown-in defects in silicon CZ growth, *J. Cryst. Growth*, 2007, **299**, 152–157.
200 T. Abe, T. Takahashi and K. Shirai, Steady distribution structure of point defects near crystal-melt interface under pulling stop of CZ Si crystal, *J. Cryst. Growth*, 2017, **459**, 87–94.
201 Y. Yoshida and G. Langouche, *Defects and Impurities in Silicon Materials: An Introduction to Atomic-Level Silicon Engineering*, Springer, 2016.
202 D. W. Oxtoby and A. D. J. Haymet, A molecular theory of the solid–liquid interface. II. Study of bcc crystal–melt interfaces, *J. Chem. Phys.*, 1982, **76**, 6262–6272.
203 M. Schmidt, R. Kusche, B. von Issendorff and H. Haberland, Irregular variations in the melting point of size-selected atomic clusters, *Nature*, 1998, **393**, 238–240.
204 G. Nasti, S. Sanchez, I. Gunkel, S. Balog and B. Roose, Patterning of perovskite–polymer films by wrinkling instabilities, *Soft Matter*, 2017, **13**, 1654–1659.
205 J. Wang, *et al.*, Templated growth of oriented layered hybrid perovskites on 3D-like perovskites, *Nat. Commun.*, 2020, **11**, 582.
206 L. A. Muscarella, *et al.*, Crystal Orientation and Grain Size: Do They Determine Optoelectronic Properties of MAPbI3 Perovskite?, *J. Phys. Chem. Lett.*, 2019, **10**, 6010–6018.
207 S. Sanchez, U. Steiner and X. Hua, Phase Evolution During Perovskite Formation—Insight from Pair Distribution Function Analysis, *Chem. Mater.*, 2019, **9**, 3498–3506.
208 *A Mechanistic Study of Phase Transformation in Perovskite Nanocrystals Driven by Ligand Passivation*, DOI: 10.1021/acs.chemmater.7b02425.s001.
209 T. J. Jacobsson, L. J. Schwan, M. Ottosson, A. Hagfeldt and T. Edvinsson, Determination of Thermal Expansion Coefficients and Locating the Temperature-Induced Phase Transition in Methylammonium Lead Perovskites Using X-ray Diffraction, *Inorg. Chem.*, 2015, **54**, 10678–10685.